CHAPTER 4

RESULTS AND DISCUSSION

4.1 $SrWO_4$ synthesized by electrospinning method

Figure.4.1.1 compares TGA curve of the M4 spider's web to that of PVA. The weight loss of pure PVA exhibited the evaporation and degradation processes for three steps over the temperature range of 32–494 ^oC. First, the weight loss of 9.5% was caused by the evaporation of loosely bound water at 32–194 ^oC. Second, the large amount of weight loss of 79.7% was predominantly due to the decomposition of PVA structure at 194–415 ^oC. Third, the 9.3% weight loss was by the breaking of PVA main chains at 415–494 ^oC. The weight loss tended to terminate upon further heating at above 494 ^oC [96]. Consider TGA curve of the M4 spider's web, the weight losses were divided into three different steps. The first weight loss at 32–218 ^oC was 15.8%, and associated with water evaporation. The second weight loss of 25.5% at 218–405 ^oC was caused by the decomposition of PVA. The final weight loss of 18.2% at 405–520 ^oC seemed to be the oxidation and decomposition of the PVA main chains. These last two steps were attributed to the loss of PVA and organic compound blended in the fibers. At a temperature above 520 ^oC, there was no significant change in their weight.

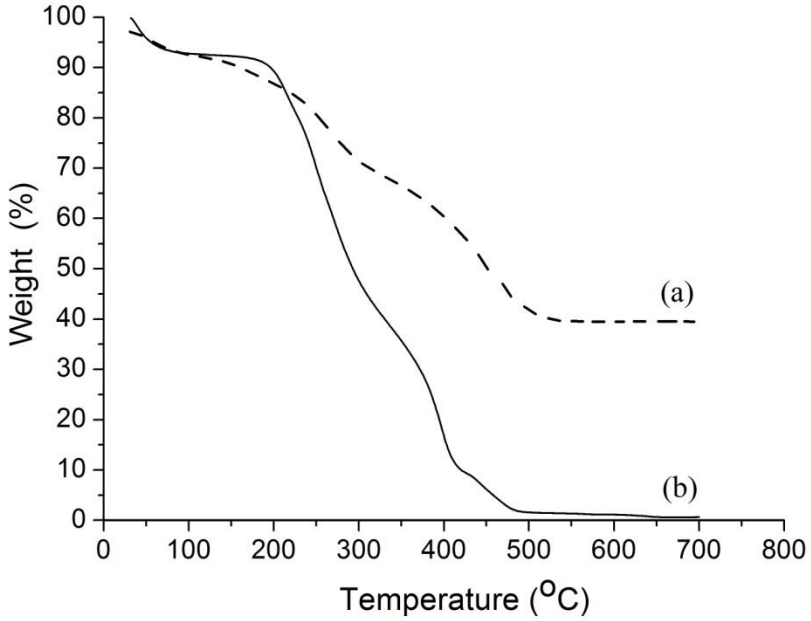

Figure 4.1.1 TGA curves of (a) a spider's web synthesized from the product prepared using PVA 1.3 g, $Sr(C_2H_3O_2)_2$ and $H_{26}N_6O_4OW_{12}{\cdot}xH_2O$ as starting reagents (Sample code M4), and (b) PVA.

Figure 4.1.2 is the representative XRD pattern of samples. All the diffraction peaks could be indexed to the tetragonal cell of $SrWO_4$, which are consistent with reported values (JCPDS file no. 00-008-0490) [91]. At 300 °C calcination, the peaks of $SrWO_4$ were quite broad. This product contained very small contents of residual PVA at 2θ = 22.50 [98], and graphite at 2θ = 26.30 of JCPDS database no. 01-0640 [99] caused by the decomposition of PVA. The product has the color of light grey, due to some graphite residue. Upon calcination at 400 °C, residual PVA and graphite were reduced, due to the evaporation of PVA and oxidation of graphite to be its oxides in gaseous form. Until at 500 °C and 600 °C calcination, they were no longer detected by the XRD. In addition, the XRD peaks became narrower and sharper, implying the improvement of products'

crystalline degree and purity. At 600 ^{o}C calcination, the product was the best pure white crystalline $SrWO_4$. Their average lattice parameters, calculated from the plane-spacing equation for tetragonal structure and Bragg's law for diffraction [100] , were a = b = 5.388 Å, and c = 11.898 Å very close to their corresponding standard values [91]. The strongest intensity peak is at 2θ = 27.83 degree and diffraction from (112) plane of the product. For scheelite structured $SrWO_4$, each Sr divalent ion was surrounded by eight O ions with each W ion in the tetrahedrons of O ions [19,87].

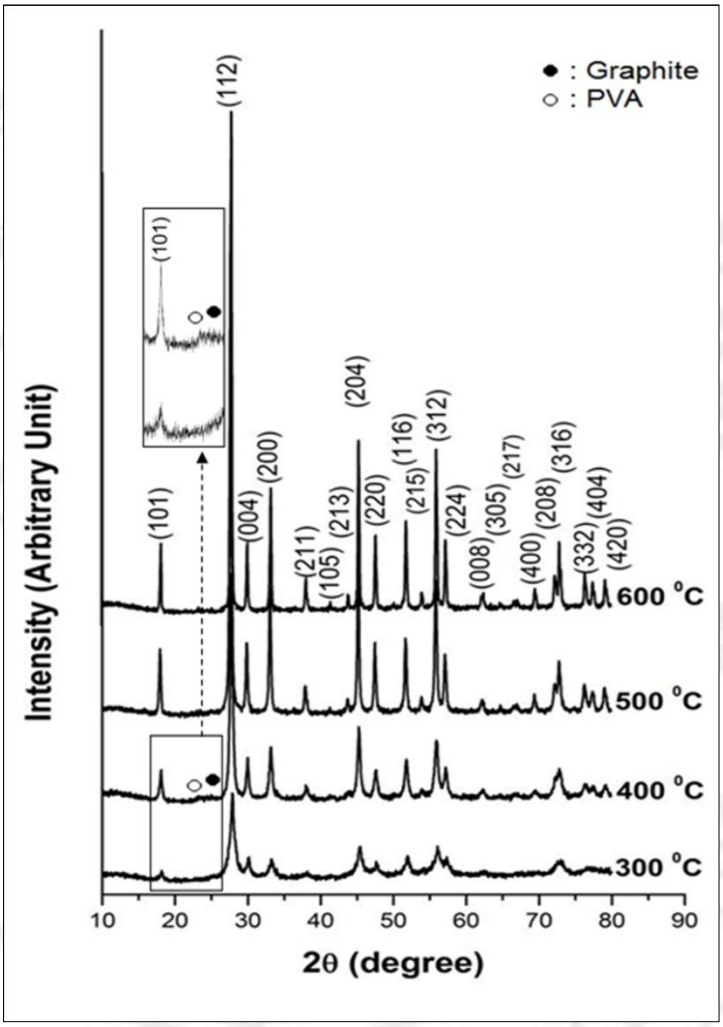

Figure 4.1.2 XRD patterns of $SrWO_4$–PVA spider's web, the product prepared using PVA 1.3 g, 4.5 mmol $Sr(C_2H_3O_2)_2$, and $H_{26}N_6O_4OW_{12}{\cdot}xH_2O$ as starting reagents (Sample code M4), after calcination at 300 ºC, 400 ºC, 500 ºC and 600 ºC for 3 h respectively.

The FTIR spectra (Figure 4.1.3) were provided further insight into the structure of PVA, and $SrWO_4$–PVA spider's web synthesized from the M4 solution, before and after calcinations at 300 ^oC, 400 ^oC, 500 ^oC and 600 ^oC for 3 h. consider the PVA spectrum, a broad strong O–H stretching mode of alcohol and residual water was detected at 3600–3200 cm^{-1}. It was the stretching of hydroxyl groups with strong hydrogen bonding of intra- and inter-types. Two strong vibration modes at 2945 and 2909 cm^{-1} corresponded to the asymmetric and symmetric C–H stretching of alkyl groups, respectively. The C=O stretching mode at 1656 cm^{-1} was caused by the carbonyl functional groups of the acetate remaining in PVA by the hydrolysis of polyvinyl acetate and oxidation process during manufacturing. The C=C stretching mode at 1566 cm^{-1} was caused by cross-linking of the PVA during heating. The presence of C=O and/or C=C stretching modes implied that PVA molecules have the same resonant structures: alkene↔alkane, and C=O↔C–O^-, or the presence of hydrogen bonds with oxygen of C=O groups. The 1439 cm^{-1} was specified as the CH_2 bending mode, the 1342 cm^{-1} as the C–CH_3 deformation vibration, and the 1241 cm^{-1} as the CH_2 wagging mode. The C–C and C–O–C stretching vibrations, recognized as the crystallization sensitive modes, were detected at 1147 cm^{-1}. The vibration at 1096 cm^{-1} was specified as the C–O stretching, and at 851 cm^{-1} as the C–C stretching [101]. Once, the as-synthesized $SrWO_4$-PVA spider's web was characterized by FTIR, additional modes of $SrWO_4$ were detected. For T_d-symmetry, vibration frequencies of $[WO_4]^{2-}$ tetrahedrons were $\nu_1(A_1)$, $\nu_2(E)$, $\nu_3(F_2)$, and $\nu_4(F_2)$ [102]. In lattice space, the site symmetries became

S_4. The correlation of the two point groups ($Td \rightarrow S_4$) is the following: $A_1 \rightarrow A$, $E \rightarrow A + B$ and $F_2 \rightarrow B + E$. Only the modes corresponding to ν_2, ν_3 and ν_4 were detected [102]. Main transmittance mode (ν_3) specified as W–O anti-symmetric stretching vibration of $[WO_4]^{2-}$ tetrahedrons in lattice space [102] was detected at 638–1003 cm^{-1}. Sometimes it split into two modes, sometimes it did not [102-104]. In the present research, they appeared as the strong broad band. The ν_4 split into two modes at the wavenumbers of less than 400 cm^{-1} [102]. When the $SrWO_4$–PVA spider's web was calcined in air at 300–600 ^oC for 3 h, the PVA and residual water began to evaporate and decompose. Additional weak peaks of W–O vibrations for 300 ^oC, 400 ^oC, 500 ^oC, and 600 ^oC were also detected at 410 cm^{-1}, specified as ν_2 bending modes [102,105]. At higher temperatures, the FTIR intensities were strengthened. The evaporation rates of PVA and water became faster, and their residues were lessened. Until at 600 ^oC calcination, the vibrations of PVA and water were no longer detected. The ν_3 anti-symmetric stretching and ν_2 bending modes became the strongest, and the product was really $SrWO_4$ electrospun nanofibrous web.

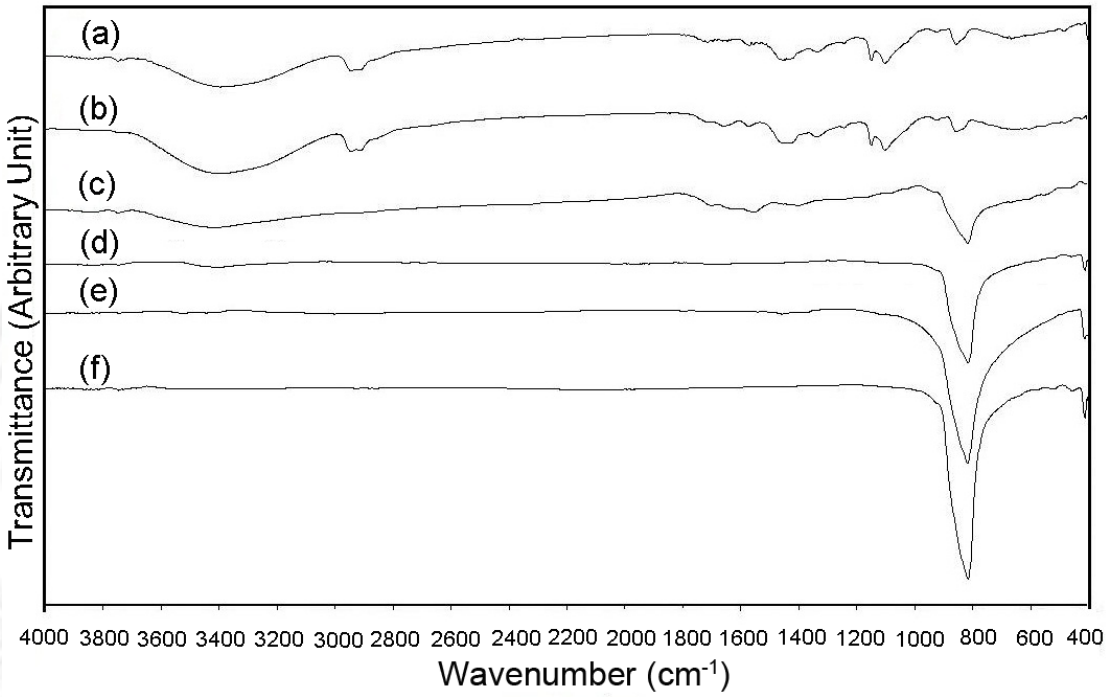

Figure 4.13 FTIR spectra of (a) PVA, and (b)–(f) $SrWO_4$–PVA spider's web, the product prepared using PVA 1.3 g, 4.5 mmol $Sr(C_2H_3O_2)_2$, and $H_{26}N_6O_4OW_{12}\cdot xH_2O$ as starting reagents (Sample code M4), before and after calcination at 300 ^oC, 400 ^oC, 500 ^oC , and 600 ^oC for 3 h respectively.

Raman spectra (Figure 4.14) revealed the presence of six vibrating bands over the range of 100–1000 cm^{-1}. The Raman vibrations of $SrWO_4$ were divided into two groups, the internal and external [106]. The internal mode was the W–O vibration within the $[WO_4]^{2-}$ tetrahedral units with immobile mass centers. The external or lattice phonon mode corresponded to the vibration of Sr^{2+} cations relative to the rigid $[WO4]^{2-}$ tetrahedral units. In free space, $[WO_4]^{2-}$ tetrahedrons have Td-symmetry [106,107]. Their vibrations were specified as four internal modes of $\nu_1(A_1)$, $\nu_2(E)$, $\nu_3(F_2)$ and $\nu_4(F_2)$, one free rotation of $\nu_{f.r.}(F_1)$, and one translation (F_2) [106]. In lattice space, they have S_4-symmetry. All degenerative vibrations were split [106,107]. Due to the crystal field effect and Davydov splitting [106]. Space,

they have S_4-symmetry. All degenerative vibrations were split [106,107] due to the crystal field effect and Davydov splitting [106]. According to group-theory calculation, there are 26 different modes for tetragonal scheelite primitive cell with zero wavevector ($\vec{k} = \vec{0}$): three for A_g and B_u, and five for A_u, B_g, E_g and E_u each. All modes of A_g, B_g and E_g were Raman-active. Four of five A_u and E_u modes were IR-active, and their remains were acoustic vibrations. Three vibrations of Bu were silent modes [106,107]. In the present research, six different modes of $\nu_1(A_g)$, $\nu_3(B_g)$, $\nu_3(Eg)$, $\nu_4(B_g)$, $\nu_2(A_g)$ and free rotation were detected on the Raman spectrum (Figure 4.14) at 912, 831, 791, 373, 334 and 187 cm^{-1} in accordance with those of the previous reports [106,107]. This spectrum provided the evidence of scheelite structure of $SrWO_4$ [106,107] spider's web. Comparing to Ar laser (λ = 514.5 nm), a great deal of energy was lost during the inelastic scattering process.

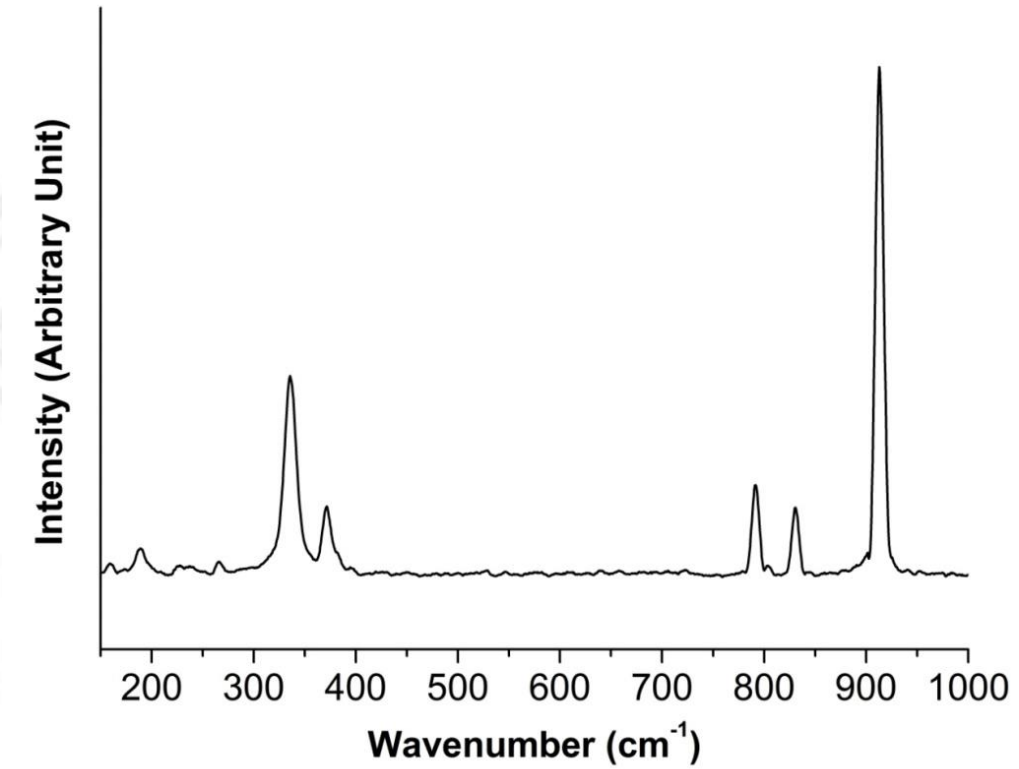

Figure 4.1.4 Raman spectrum of $SrWO_4$ spider's web, the product prepared using PVA 1.3 g, 4.5 mmol $Sr(C_2H_3O_2)_2$, and $H_{26}N_6O_4OW_{12}{\cdot}xH_2O$ as starting reagents (Sample code M4), after calcination 600 ^oC for 3 h.

SEM images of the $SrWO_4$ –PVA spiders' webs synthesized from the solutions containing different contents of PVA are shown in Figure 4.15-4.18. The spiders' webs of the M1, M2, M3, and M4 solutions, respective containing 1.0, 1.1, 1.2, and 1.3 g PVA, were composed of fibers woven like spiders' webs. Some beads were also detected; especially, those synthesized from the mixtures of less than 1.3 g PVA. The number of beads was lessened in sequence with the increase of the PVA masses, and was no longer detected for 1.3 g PVA (M4) solution. The content of PVA can also play the role in the viscosity of the mixtures, which influenced the stability of the solution jets. For 1.3 g PVA,

it was exactly right to eject the inorganic material-polymeric solution through the syringe out of the hollow needle, and the web was composed of the bead-free fibers. These implied that the fibers and beads were influenced by the stability of the jet of inorganic material-polymeric solutions, and PVA contents [5,109]. The M4 spider's web was then selected for further studies. When the $SrWO_4$–PVA spider's web was calcined at 300–600 ^oC for 3 h (Figure 4.1.9-4.1.12), the fibers became thinner, due to the evaporation and decomposition of PVA and 600 ^oC for 3 h volatile components. $SrWO_4$ nuclei also grew to form larger nanoparticles. Upon increasing the calcination temperatures, the evaporation and decomposition rates of PVA, as well as the growth rate of $SrWO_4$ nanoparticles, were increased. It was more than likely that PVA did not remain in the products with 500 ^oC and 600 ^oC calcination. These products were composed of nanoparticles with different sizes and orientations joined together like a spider's web.

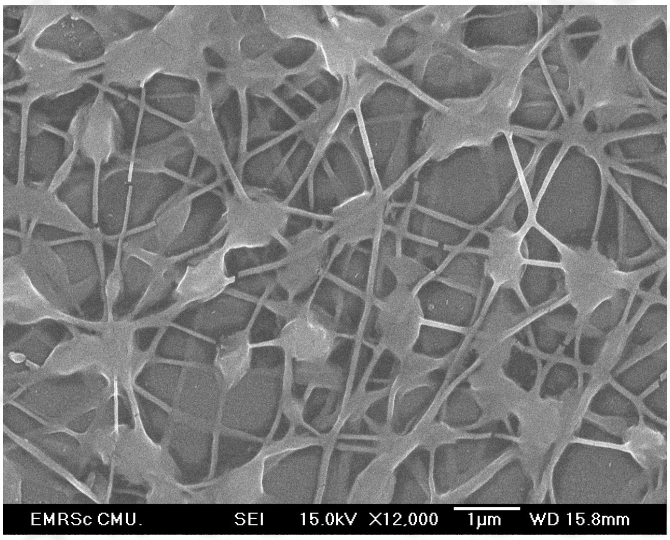

Figure 4.1.5 SEM image the product prepared using PVA 1.0 g, 4.5 mmol $Sr(C_2H_3O_2)_2$ and $H_{26}N_6O_4OW_{12}\cdot xH_2O$ as starting reagents (Sample code M1).

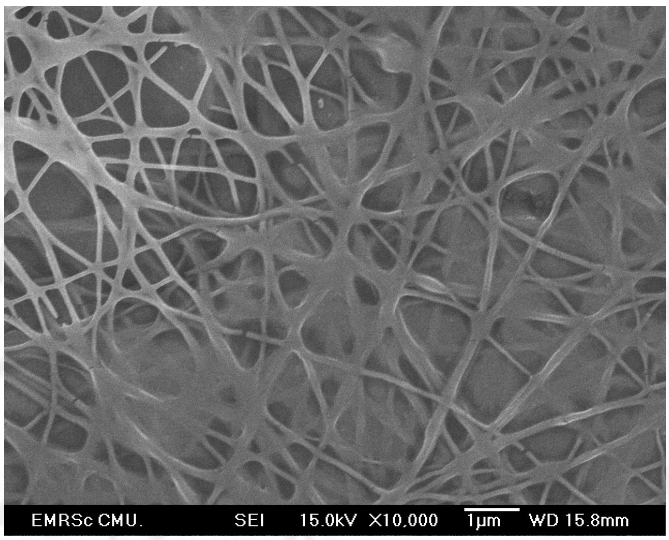

Figure 4.1.6 SEM image of the product prepared using PVA 1.1 g, 4.5 mmol $Sr(C_2H_3O_2)_2$ and $H_{26}N_6O_4OW_{12}\cdot xH_2O$ as starting reagents (Sample code M2).

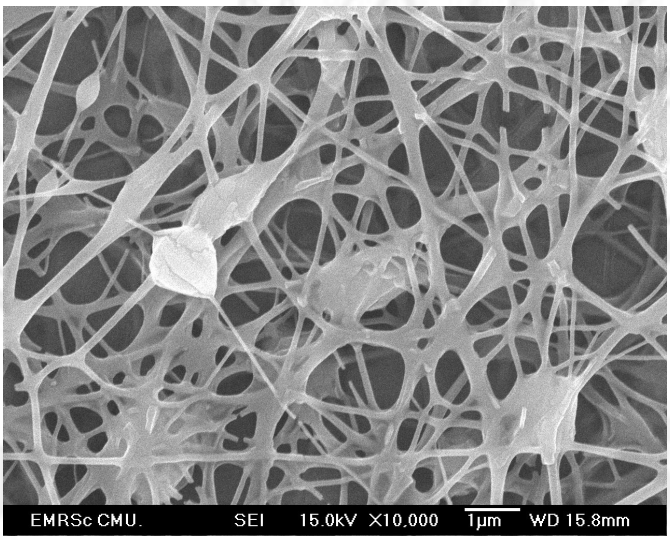

Figure 4.1.7 SEM image of the product prepared using PVA 1.2 g, 4.5 mmol $Sr(C_2H_3O_2)_2$ and $H_{26}N_6O_4OW_{12}\cdot xH_2O$ as starting reagents (Sample code M3).

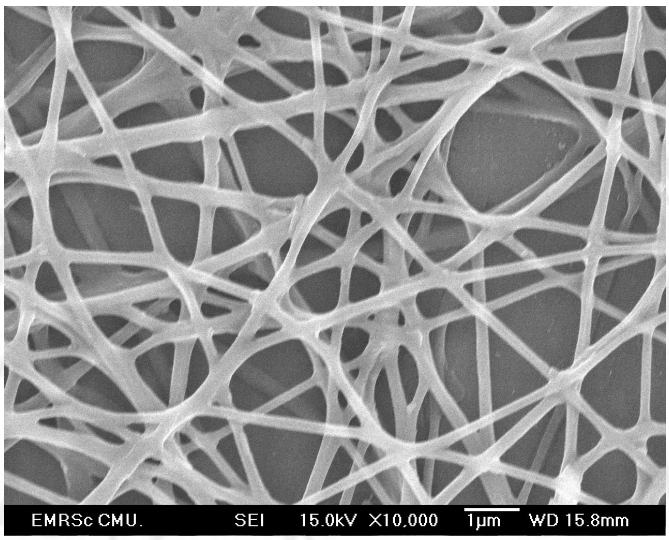

Figure 4.1.8 SEM image of the product prepared using PVA 1.3 g, 4.5 mmol $Sr(C_2H_3O_2)_2$ and $H_{26}N_6O_4OW_{12}\cdot xH_2O$ as starting (Sample code M4).

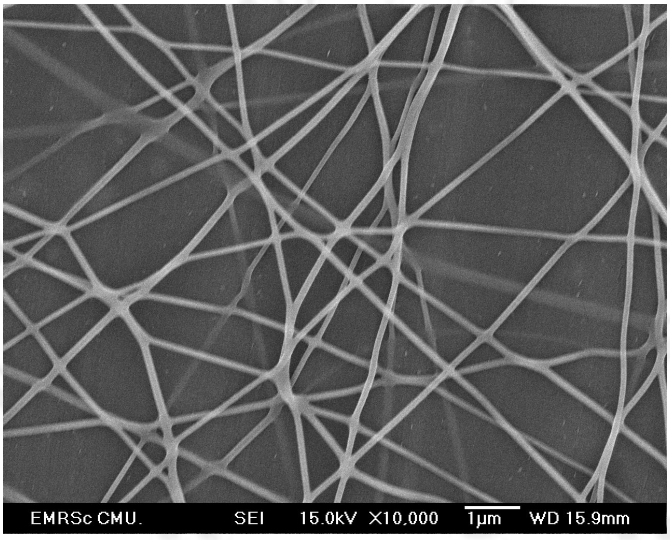

Figure 4.1.9 SEM image of the product prepared using PVA 1.3 g, 4.5 mmol $Sr(C_2H_3O_2)_2$ and $H_{26}N_6O_4OW_{12}\cdot xH_2O$ as starting reagents (Sample code M4) calcined at 300 ^oC for 3 h.

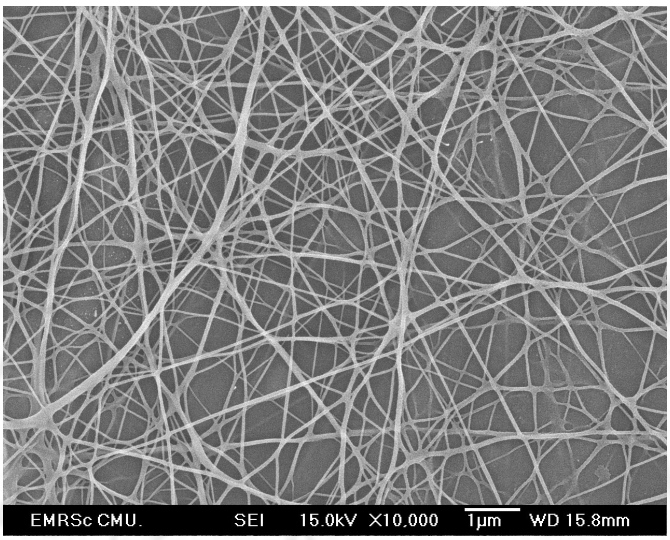

Figure 4.1.10 SEM image of the product prepared using PVA 1.3 g, 4.5 mmol $Sr(C_2H_3O_2)_2$ and $H_{26}N_6O_4OW_{12}\cdot xH_2O$ as starting reagents (Sample code M4), calcined at 400 ^oC for 3 h.

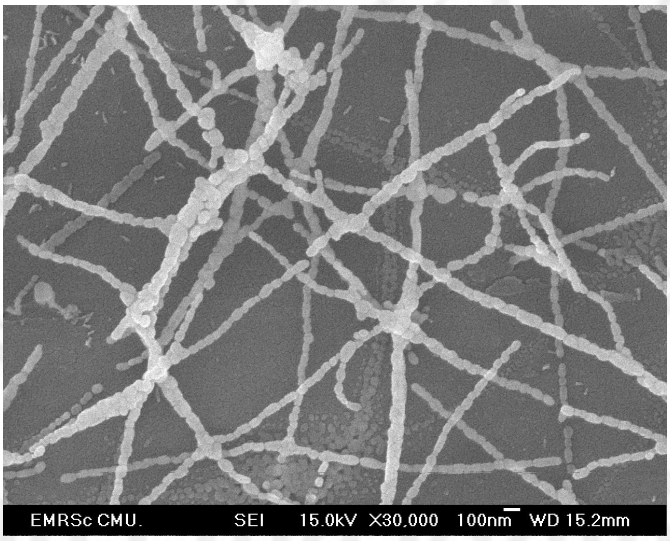

Figure 4.1.11 SEM image of the product prepared using PVA 1.3 g, 4.5 mmlo $Sr(C_2H_3O_2)_2$ and $H_{26}N_6O_4OW_{12}\cdot xH_2O$ as starting reagents (Sample code M4), calcined at 500 ^oC for 3 h.

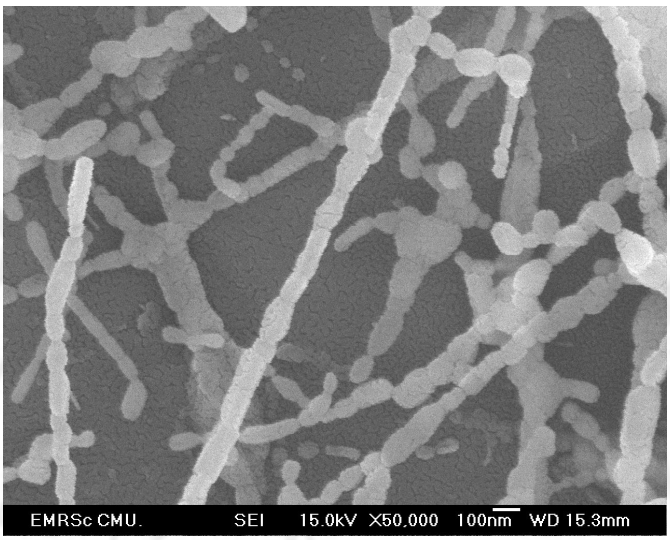

Figure 4.1.12 SEM image of the product prepared using PVA 1.3 g, 4.5 mmol $Sr(C_2H_3O_2)_2$ and $H_{26}N_6O_4OW_{12}\cdot xH_2O$ as starting reagents (Sample code M4), calcined at 600 ^oC for 3 h.

TEM images, HRTEM and SAED patterns (Figure 4.1.13 – Figure 4.1.15) of the products with 500 ^oC and 600 ^oC calcinations. For close examination on a nanoparticle calcined at 500 ^oC, a number of parallel crystallographic planes were detected by HRTEM (Figure 4.1.13b). They were specified as the (1 0 1) plane of tetragonal structured $SrWO_4$, implying that the nanoparticle was really a single crystal. SAED patterns were interpreted [110], and specified at the (101), (112) and (011) planes (Figure 4.1.14a) with electron beam in the $[\bar{1}\bar{1}1]$ direction, and the (200), (220) and (020) planes (Figure 4.1.14d) with electron beam in the [0 0 1] direction for the nanoparticles of 500 ^oC and 600 ^oC calcination, respectively. They corresponded to the JCPDS database for tetragonal structured $SrWO_4$ [91] in good accordance with the above XRD analysis. Diffraction patterns of these products (Figure 4.1.14b and Figure 4.1.15b) were also simulated

[111] using the corresponding electron beams. They are in systematic and symmetric order, with the a*, b* and c* reciprocal lattice vectors for both patterns in the [100], [010], and [001] directions. For one crystal structure, the corresponding reciprocal lattice vectors were the same although the electron beams were different. Comparing between the corresponding interpreted and simulated patterns, they are in good accordance.

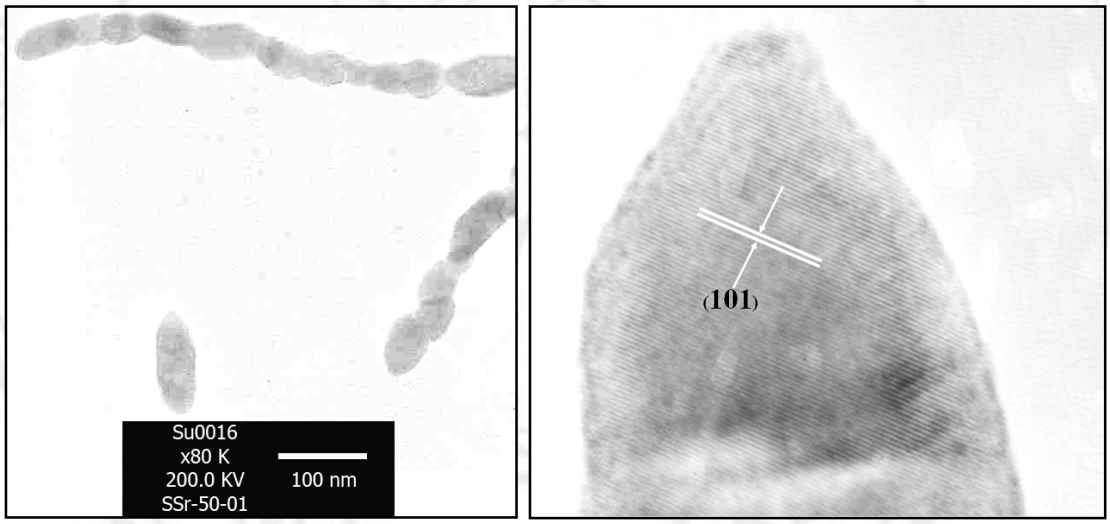

(a) (b)

Figure 4.1.13 TEM and HRTEM images, of $SrWO_4$–PVA spider's web, synthesized from the product prepared using PVA 1.3 g, 4.5 mmol $Sr(C_2H_3O_2)_2$ and $H_{26}N_6O_4OW_{12}{\cdot}xH_2O$ as starting reagents (Sample code M4), after calcination at (a and b) 500 ^oC for 3 h.

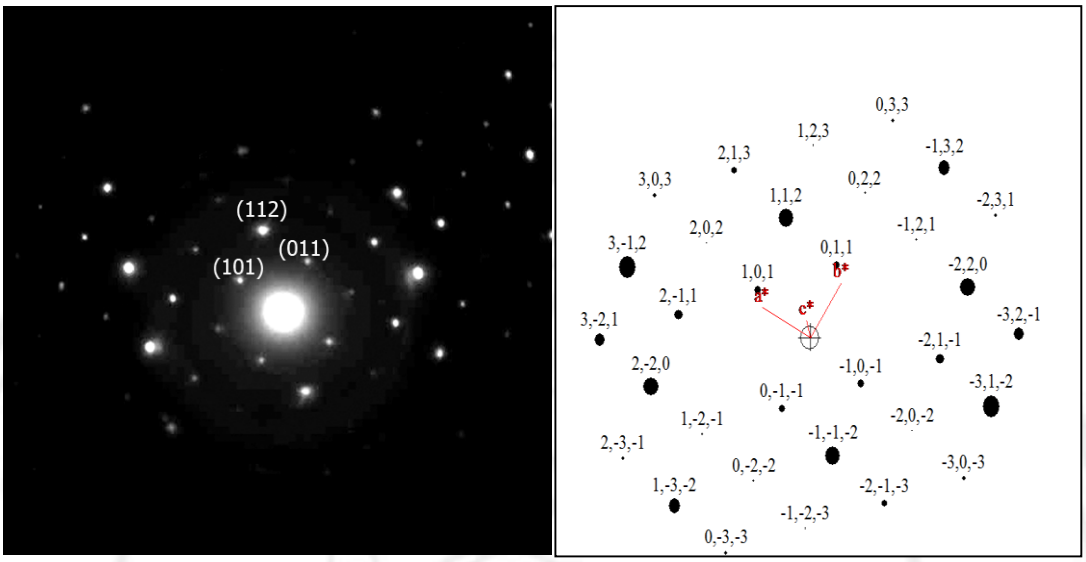

(a) (b)

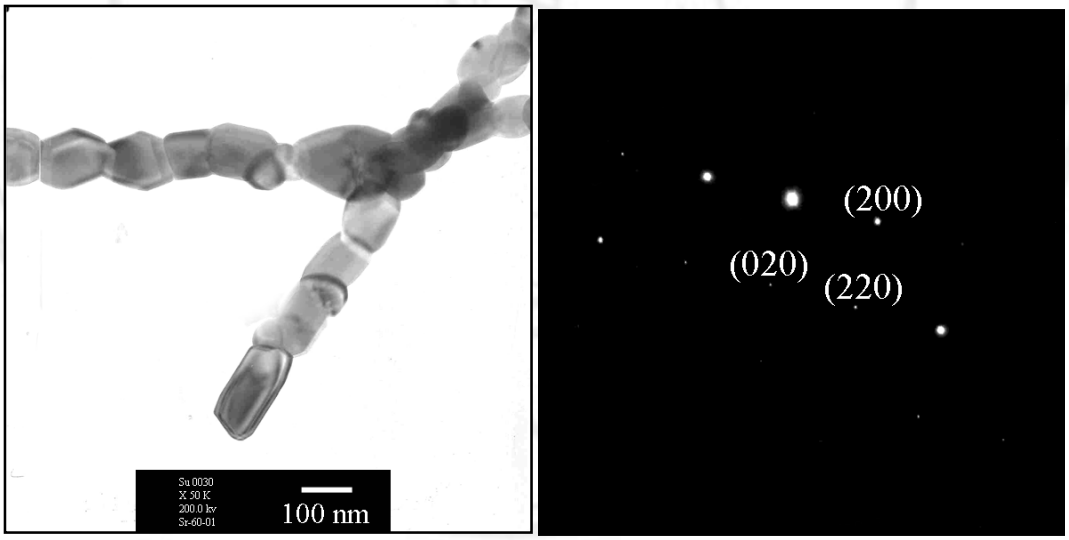

(c) (d)

Figure 4.1.14 SAED and simulated patterns, TEM images and SAED of $SrWO_4$–PVA spider's web, synthesized from the product prepared using PVA 1.3 g, $Sr(C_2H_3O_2)_2$ and $H_{26}N_6O_4OW_{12}{\cdot}xH_2O$ as starting reagents (Sample code M4), after calcination at (a and b) 500 ^oC, and (c and d) 600 ^oC for 3 h.

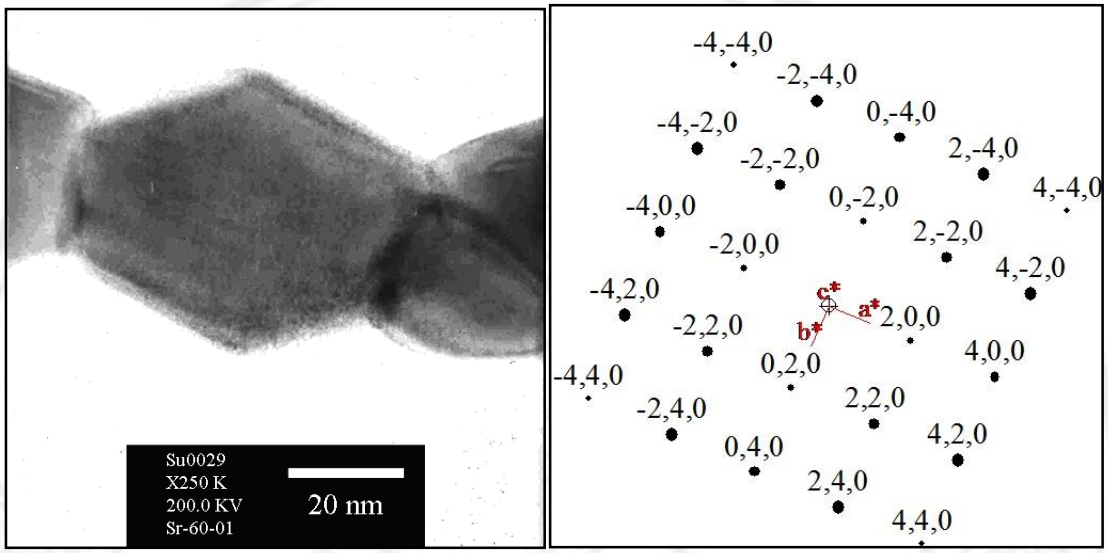

(a) (b)

Figure 4.1.15 TEM images and SAED of $SrWO_4$–PVA spider's web, the product prepared using PVA 1.3 g, $Sr(C_2H_3O_2)_2$ and $H_{26}N_6O_4OW_{12}{\cdot}xH_2O$ as starting reagents (Sample code M4), after calcination at (a and b) 600 ºC for 3 h.

Distributions of fibrous diameters and particle sizes of the spider's web, synthesized from the M4 solution, before and after calcination at 600 ^{o}C for 3 h are shown in Figure 4.1.16 These fibrous diameters and particle sizes were started to be counted and arranged from the smallest to the largest values. Their distributions fitted very well with normal curves over the ranges of 60–320 nm with the average of 185.6 nm diameter, and 20–150 nm with the average of 82.3 nm particle size.

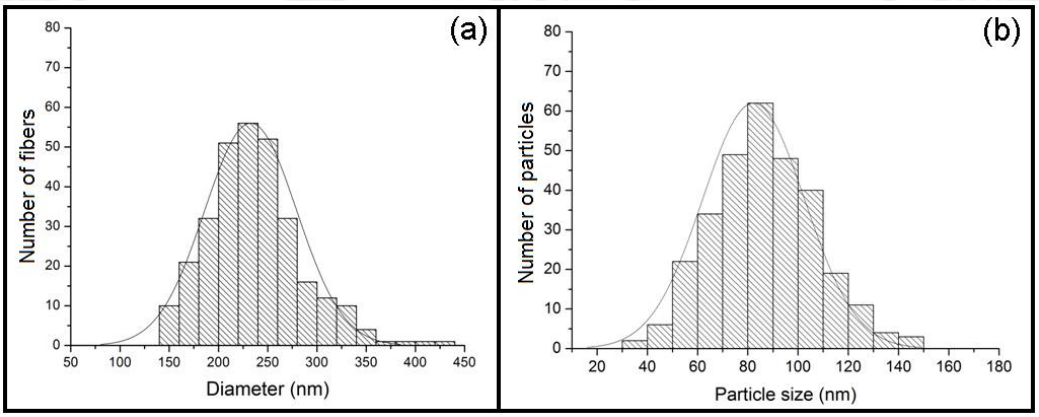

Figure 4.1.16 (a) and (b) Distributions of fibrous diameters and particle sizes of the $SrWO_4$–PVA spider's web, the product prepared using PVA 1.3 g, 4.5 mmol $Sr(C_2H_3O_2)_2$ and $H_{26}N_6O_4OW_{12}\cdot xH_2O$ as starting reagents (Sample code M4), before and after calcination at 600 ^{o}C for 3 h.

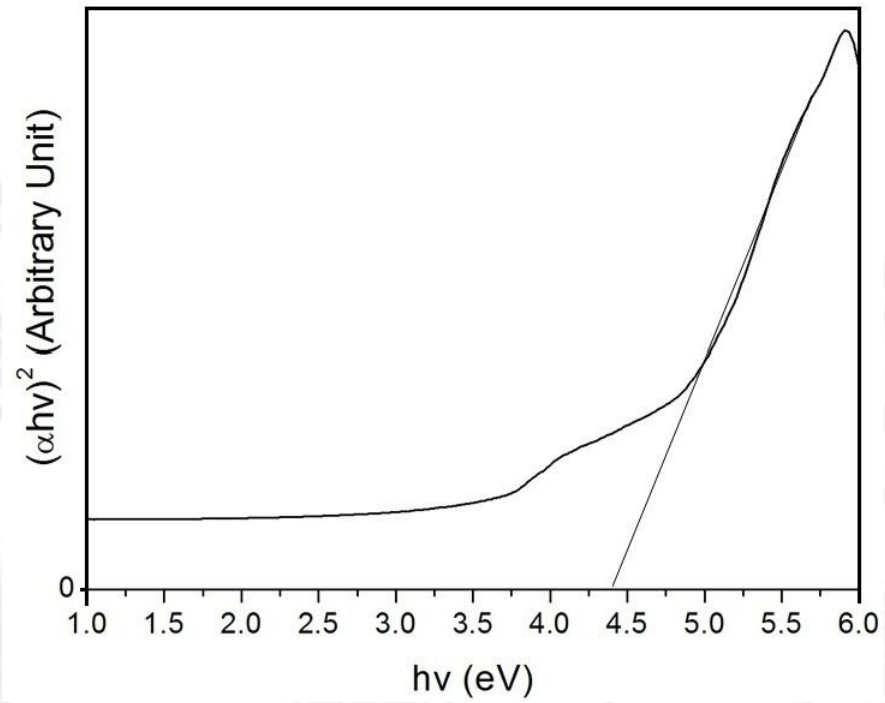

Figure 4.1.17 The $(\alpha hv)^2$ versus hv plot of the $SrWO_4$ spider's web, the product prepared using PVA 1.3 g, 4.5 mmol $Sr(C_2H_3O_2)_2$ and $H_{26}N_6O_4OW_{12}{\cdot}xH_2O$ as starting reagents (Sample code M4).

Figure 4.17 shows the $(\alpha hv)^2$ vs hv curve of the $SrWO_4$ spider's eb. By using Wood and Tauc equation [19,87,112-114] below.

$$\alpha hv = (hv - E_g)^n \qquad (4.2)$$

where α is the absorbance, h the Planck constant, n the photon frequency, E_g the energy gap, and n the pure numbers associ-ated with the different types of electronic transitions. For $n = 1/2, 2, 3/2$ and 3, the transitions are the direct allowed, indirect allowed, direct forbidden, and indirect forbidden, respectively. It should be noted that the absorption was controlled by two photon energy (hv) ranges—the high and low energies. When the photon

energy was greater than the energy band gap, absorption was linearly increased with the increasing of photon energy. The steep inclination of the linear portion of the curve was caused by the UV absorption for charged transition from the topmost occupied state of valence band to the bottommost unoccupied state of the conduction band. For the photon energy with less than the energy band gap, the absorption curve became different from linearity, due to the UV absorption for charged transition relating to different defects. The direct energy gap (E_g) was determined by extrapolating the linear portion of the curve to the zero absorbance. In the present research, $SrWO_4$ with scheelite-type tetragonal structure presented the direct allowed electronic transition [19,112,113], with the energy gap of 4.47 eV in good accordance with the previous reports [87]. In fact, energy gap is controlled by several factors such as the electronegativity of transition metal ions, connectivity of the polyhedrons, deviation in the O–W–O bonds, distortion of the $[WO_4]^{2-}$ tetrahedrons, growth mechanism, and degree of structural order-disorder in the lattice [87, 112].

PL spectra of $SrWO_4$–PVA spider's web, synthesized from the M4 solution, after calcination at 300 ^oC, 400 ^oC, 500 ^oC and 600 ^oC for 3 h (Figure 4.1.18) show the intrinsic peaks with their surrounding shoulders. The intrinsic peaks were due to the $^1T_2 \rightarrow {}^1A_1$ transition of electrons within $[WO_4]^{2-}$ anions [115,116], which were treated as excitons. The shoulders were caused by some defects and/or impurities, and interpreted as extrinsic transition. Generally, PL intensity is controlled by the number of charged transition. In the present research, the emission peaks were in the spectral region at 439–441 nm having the potential applications for photonic sensors and devices. Starting from 300 ^oC

to 600 ^{o}C calcination, PL intensities were 74, 89, 98, and 100%, respectively. They were increased with the increase in the calcination temperatures, and became the highest at 600 ^{o}C calcination.

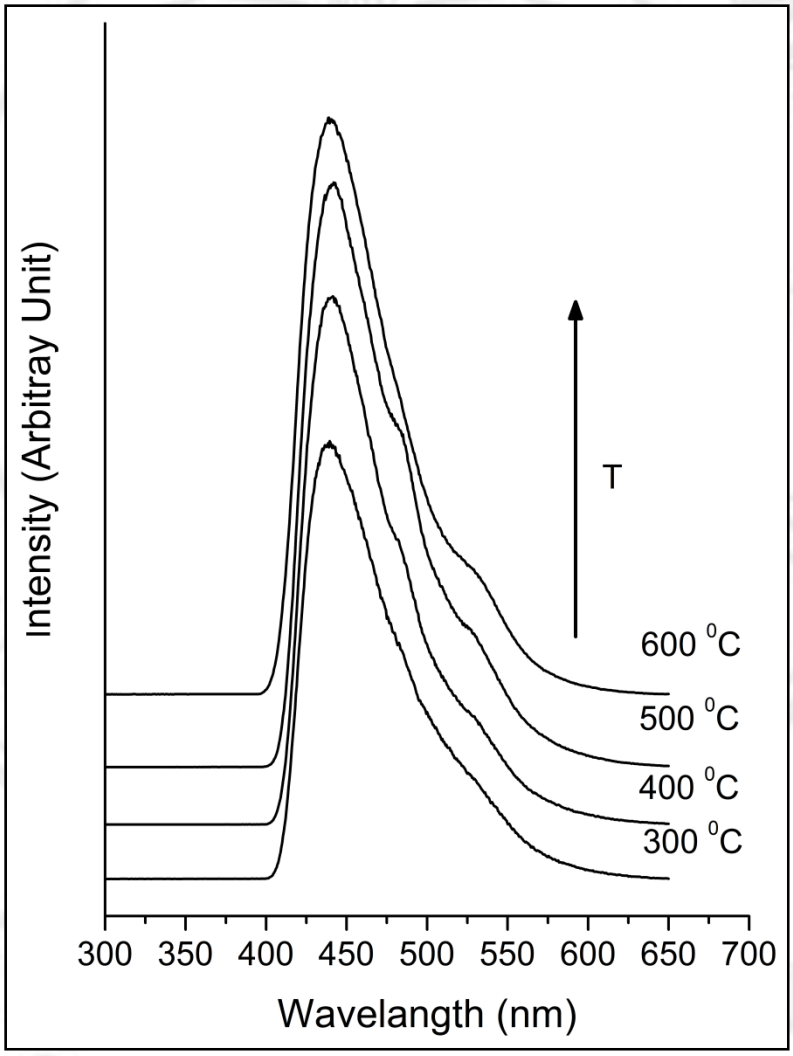

Figure 4.1.18 PL spectra of $SrWO_4$–PVA spider's web, the product prepared using PVA 1.3 g, 4.5 mmol $Sr(C_2H_3O_2)_2$ and $H_{26}N_6O_4OW_{12}{\cdot}xH_2O$ as starting reagents (Sample code M4), after calcination at 300 ^{o}C, 400 ^{o}C, 500 ^{o}C and 600 ^{o}C for 3 h, respectively.

4.2 $MgWO_4$ synthesized by electrospinning method

Figure 4.2.1 is the representative XRD pattern of samples of the MW5C1, MW5C2 and MW5C3 products show that chemical reactions of the starting materials were completed $MgWO_4$ with anorthic (JCPDS no. 00-045-0412) [92] and monoclinic (JCPDS no. 01-072-2191) [93] were successfully synthesized. During electrospinning by a +15 kV direct voltage, $(CH_3COO)_2$ $Mg{\cdot}4H_2O$ reacted with $(NH_4)_6W_7O_{24}{\cdot}4H_2O$ to synthesize $MgWO_4$ molecules, blended in the PVA template.

$$7Mg^{2+} + (W_7O_{24})^{6-} + 4H_2O \rightarrow 7MgWO_4 + 8H^+ \qquad (4.2)$$

$(CH_3COO)_2Mg{\cdot}4H_2O$ and $(NH_4)_6W_7O_{24}{\cdot}4H_2O$ could remain in the template but their concentrations were too low to be detected by XRD. By calcination at 500 ^oC for 3 h, PVA evaporated and decomposed. The PVA was no longer detected at 494 ^oC and above [117]. At the same time, the $(CH_3COO)_2$ $Mg{\cdot}4H_2O$ and $(NH_4)_6W_7O_{24}{\cdot}4H_2O$ residues combined to form $MgWO_4$ molecules, which nucleated and grew to be particles (mixed phases) with different orientations. Upon increasing of the calcination temperature to 600 ^oC, the anorthic phase became lessened, with the greater extent of the monoclinic one. At 700 ^oC and 3 h calcination, only the monoclinic crystal structure was detected, and the product was the best crystal – the atoms resided in perfect crystal lattice. Its calculated lattice parameters [100] (Table 4.2.1) were very close to those of the standard values [93], which supported the presence of $MgWO_4$ with monoclinic crystal system. By using the Scherrer formula [100], crystallite sizes of the MW5C1, MW5C2 and MW5C3 products were calculated and summarized in Table 4.2.1 Crystallite sizes of both anorthic and monoclinic phases were increased with the increasing in the calcination temperatures,

but the rate of increasing for the first was slower than that for the second. It should be noted that the anorthic crystallites were smaller than the monoclinic ones.

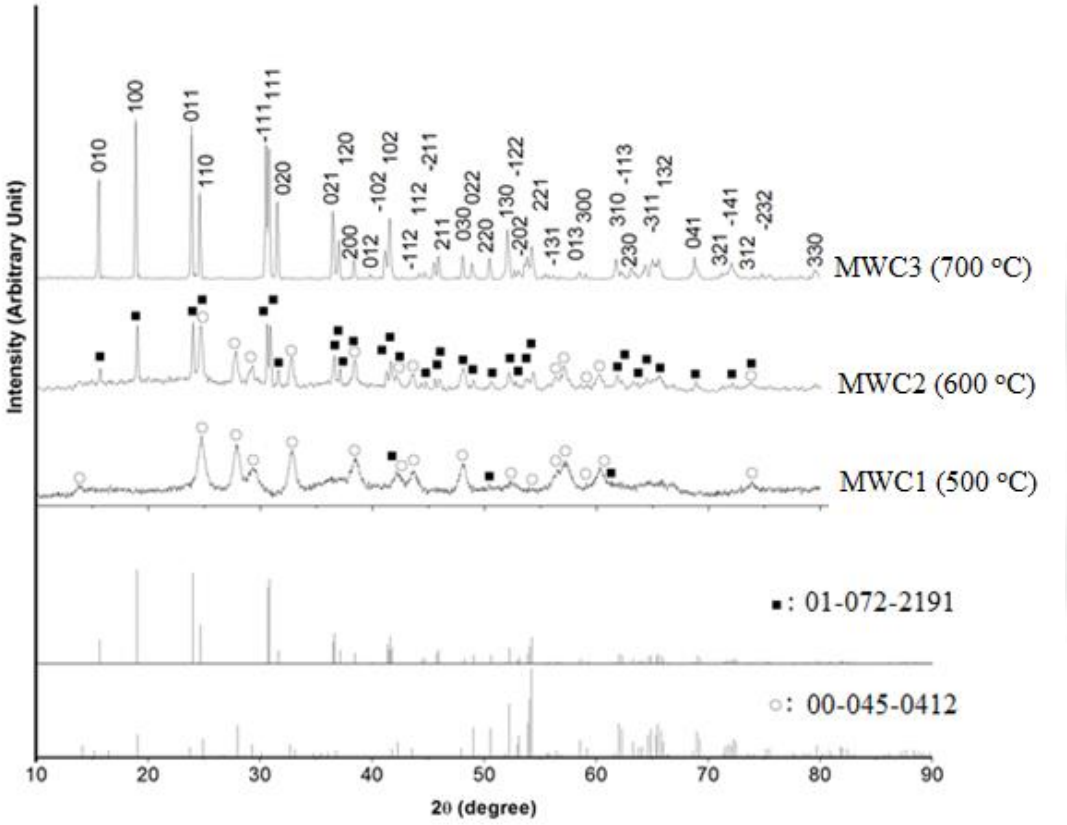

Figure 4.2.1 XRD spectra of the MW5C1, MW5C2, and MW5C3 products, compared with the anorthic and monoclinic $MgWO_4$ phases, the product prepared using PVA 1.3 g, 4.5 mmol $(CH_3COO)_2Mg{\cdot}4H_2O$ and $H_{26}N_6O_4OW_{12}{\cdot}xH_2O$ as starting reagents, after calcination at 500 ^oC, 600 ^oC, and 700 ^oC for 3 h respectively.

Table 4.2 Lattice parameters and crystallite sizes of the MW5C1, MW5C2 and MW5C3, the product prepared using PVA 1.3 g, 4.5 mmol $(CH_3COO)_2Mg{\cdot}4H_2O$ and $H_{26}N_6O_4OW_{12}{\cdot}xH_2O$ as starting reagents, after calcination at 500 ^oC, 600 ^oC, and 700 ^oC for 3 h respectively.

Product	Lattice parameter (nm)			Crystallite size (nm)	
	a	b	c	Anorthic	Monoclinic
MW5C1	-	-	-	15.0	23.0
MW5C2	-	-	-	29.6	68.8
MW5C3	0.465	0.564	0.490	–	69.8

XRD pattern of monoclinic $MgWO_4$ was simulated [111] as shown in Figure 1b. In the present research, the 2Θ Bragg's angles and peak intensities of the experiment, simulation and JCPDS database were in good accordance. Simulated crystal structure of monoclinic $MgWO_4$ (inset of Figure 4.2.2.) was explained as network of

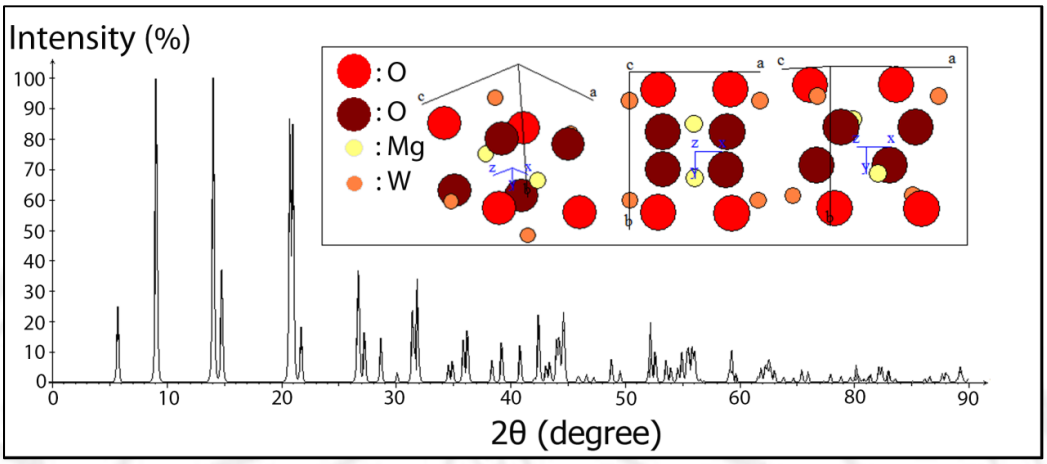

Figure 4.2.2 Simulated XRD pattern and crystal structure of monoclinic $MgWO_4$, the product prepared using PVA 1.3 g, 4.5 mmol $(CH_3COO)_2Mg{\cdot}4H_2O$ and $H_{26}N_6O_4OW_{12}{\cdot}xH_2O$ as starting reagents, after calcination 700 ^oC for 3 h.

Figure 4.2.3-4.2.12 are the representative SEM show external surfaces of the products electrospun from different contents of the starting materials, before and after calcination at 500, 600, and 700 ^oC for 3 h constant length of time. Before calcination, some beads were detected on the MW1 and MW2 products (Figure 4.2.3 and 4.2.4) but no longer detected on the MW3 product (Figure 4.2.5). Upon increasing the amount of PVA, the beads became lessened. Finally, they were no longer detected. These showed that the increase of viscosity of the mixtures played the role in the absence of beads on the electrospun fibers. The mixture of 1.5 mmol $(CH_3COO)_2Mg{\cdot}4H_2O$), 1.5 mmol $(NH_4)_6W_7O_{24}{\cdot}4H_2O$ and 1.3 g PVA has the viscosity and density high enough to form the bead-free electrospun fibers. By increasing the amount of the starting materials but keeping the amount of PVA constant at 1.3 g, the products were still to be bead-free electrospun fibers (Figure 4.2.7 and 4.2.9). $MgWO_4$ molecules and nanoparticles in the fibers became denser, proved by the

MW3C1, MW4C1 and MW5C1 products (Figure 4.2.6, 4.2.8h, and 4.2.10). Surfaces of the fibers were roughened. The products were composed of interconnecting of facet nanoparticles along the fibrous axes. Upon increasing the calcination temperature of the MW5C1 product from 500 ºC to 600 ºC (MW5C2) and 700 ºC (MWC3) (Figure 4.2.10, 4.2.11, and 4.2.12), both the nanoparticles and fibers were enlarged.

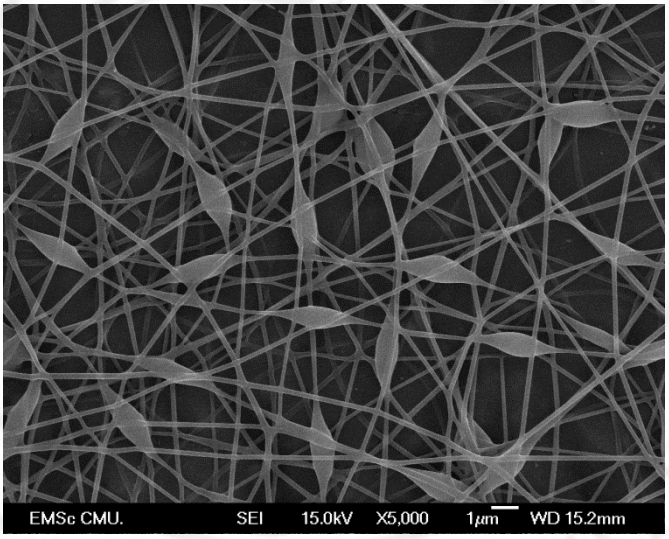

Figure 4.2.3 SEM image of the product prepared using 1.5 mmol $(CH_3COO)_2Mg{\cdot}4H_2O$, $(NH_4)_6W_7O_{24}{\cdot}4H_2O$, and PVA 0.9 g as starting reagents (Sample code MW1).

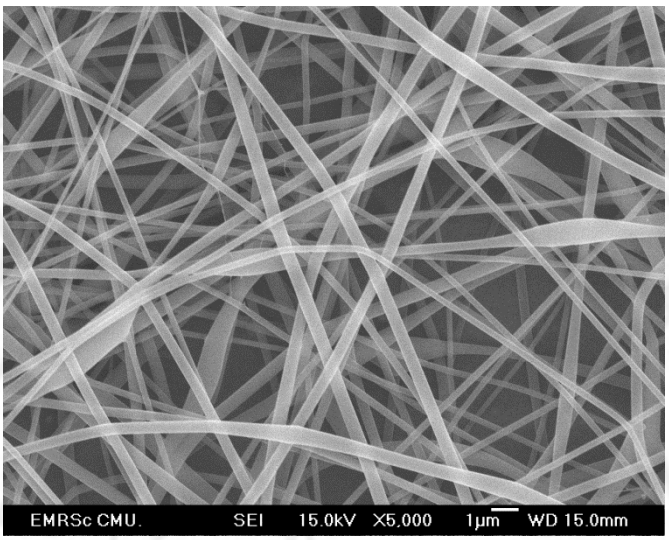

Figure 4.2.4 SEM image of the product prepared using 1.5 mmol $(CH_3COO)_2Mg{\cdot}4H_2O$, $(NH_4)_6W_7O_{24}{\cdot}4H_2O$, and PVA 1.1 g as starting reagents (Sample code MW2).

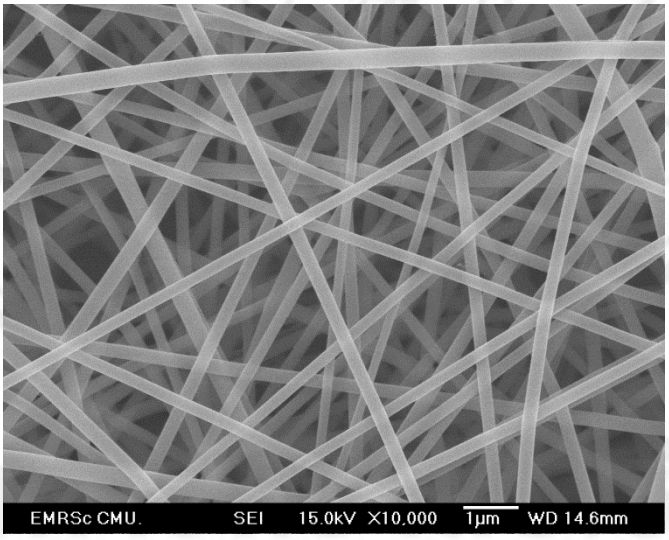

Figure 4.2.5 SEM image of the product prepared using 1.5 mmol $(CH_3COO)_2Mg{\cdot}4H_2O$, $(NH_4)_6W_7O_{24}{\cdot}4H_2O$, and PVA 1.3 g as starting reagents (Sample code MW3).

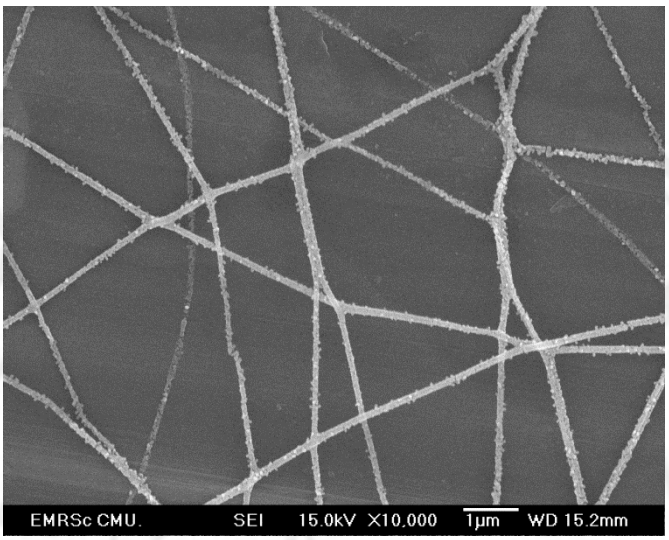

Figure 4.2.6 SEM image of the product prepared using 1.5 mmol $(CH_3COO)_2Mg{\cdot}4H_2O$, $(NH_4)_6W_7O_{24}{\cdot}4H_2O$, and PVA 1.3 g as starting reagents and calcination at 500 ^oC for 3 h (Sample code MW3C1).

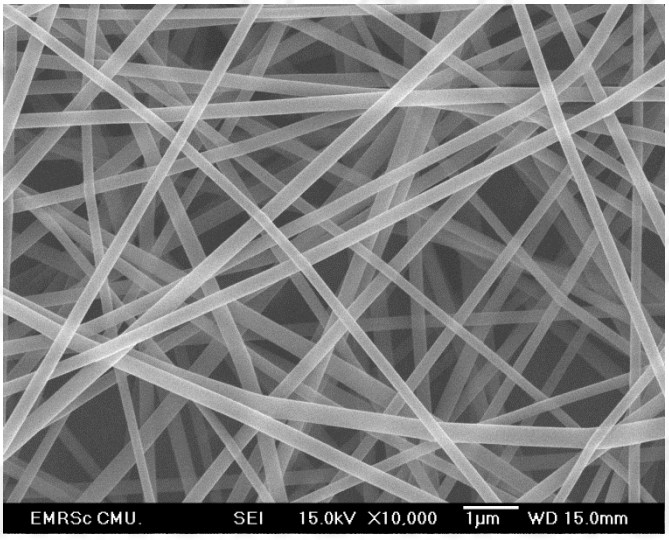

Figure 4.2.7 SEM image of the product prepared using 3.0 mmol $(CH_3COO)_2Mg{\cdot}4H_2O$, $(NH_4)_6W_7O_{24}{\cdot}4H_2O$, and PVA 1.3 g as starting reagents (Sample code MW4).

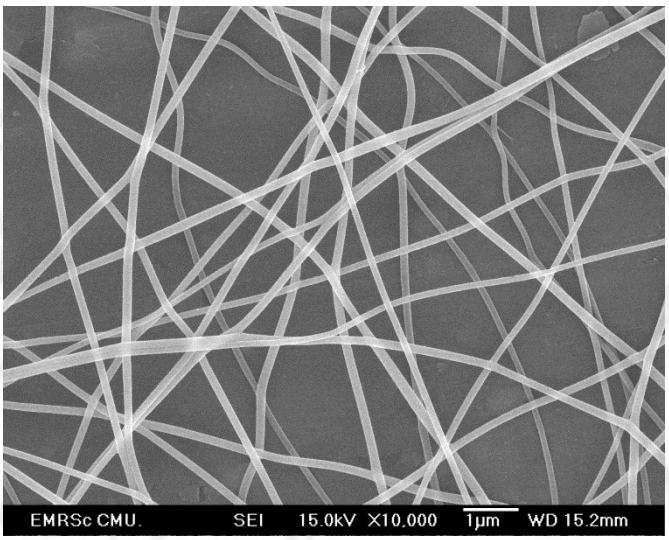

Figure 4.2.8 SEM image of the product prepared using 3.0 mmol $(CH_3COO)_2Mg{\cdot}4H_2O$, $(NH_4)_6W_7O_{24}{\cdot}4H_2O$, and PVA 1.3 g as starting reagents and calcination at 500 ^oC for 3 h (Sample code MW4C1).

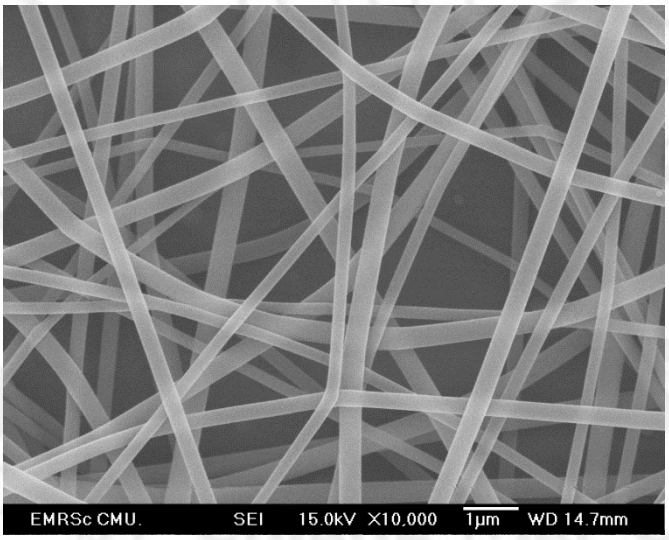

Figure 4.2.9 SEM image of the product prepared using 4.5 mmol $(CH_3COO)_2Mg{\cdot}4H_2O$, $(NH_4)_6W_7O_{24}{\cdot}4H_2O$, and PVA 1.3 g as starting reagents (Sample code MW5).

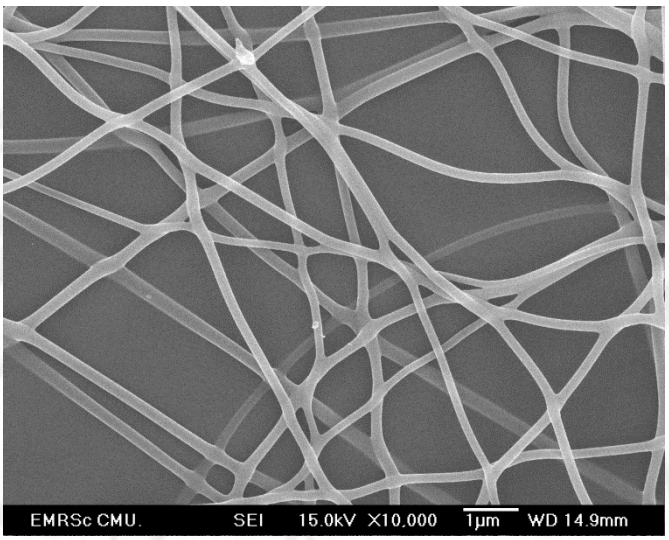

Figure 4.2.10 SEM image of the product prepared using 4.5 mmol $(CH_3COO)_2Mg{\cdot}4H_2O$, $(NH_4)_6W_7O_{24}{\cdot}4H_2O$, and PVA 1.3 g as starting reagents and calcination at 500 ^oC for 3 h (Sample code MW5C1).

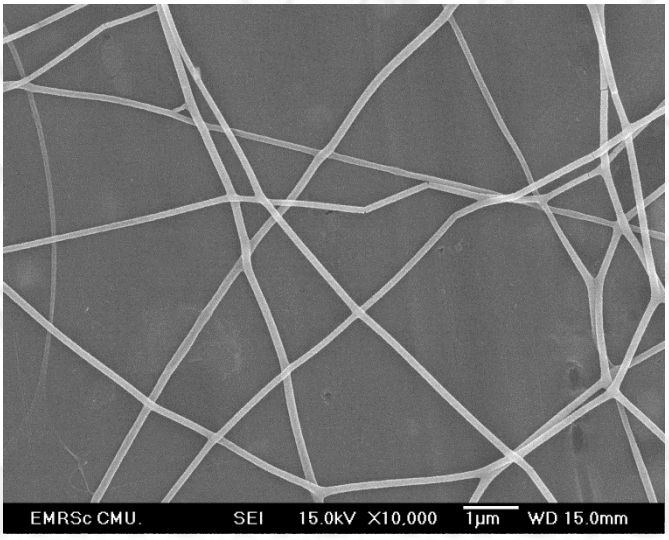

Figure 4.2.11 SEM image of the product prepared using 4.5 mmol $(CH_3COO)_2Mg{\cdot}4H_2O$, $(NH_4)_6W_7O_{24}{\cdot}4H_2O$, and PVA 1.3 g as starting reagents and calcination at 600 ^oC for 3 h (Sample code MW5C2).

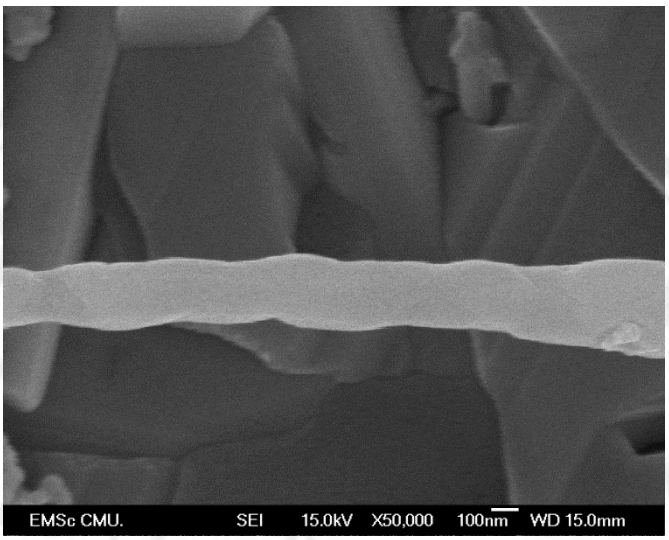

Figure 4.2.12 SEM image of the product prepared using 4.5 mmol $(CH_3COO)_2Mg{\cdot}4H_2O$, $(NH_4)_6W_7O_{24}{\cdot}4H_2O$, and PVA 1.3 g as starting reagents and calcination at 700 ^oC for 3 h (Sample code MW5C3).

TEM images, HRTEM and SAED patterns (Figure 4.2.13 and Figure 4.2.14). The products were composed of interconnecting of facet nanoparticles along the fibrous axes. Upon increasing the calcination temperature of the MW5C1 product from 500 ^oC to 700 ^oC (MW5C3) (Figure 4.2.13 c, and Figure 4.2.14 a and b), both the nanoparticles and fibers were enlarged. A number of the (0 1 0) crystallographic planes of typical nanoparticles of the MW3C1 and MW5C1 products (insets of Figure 4.2.13 b and d) were detected by HRTEM – revealing the presence of crystalline $MgWO_4$ in the fibers. A SAED pattern of the MW5C3 product (Figure 4.2.14 c) corresponded to the database of the monoclinic $MgWO_4$ [93], and the pattern obtained by simulation (Figure 4.2.14 d)

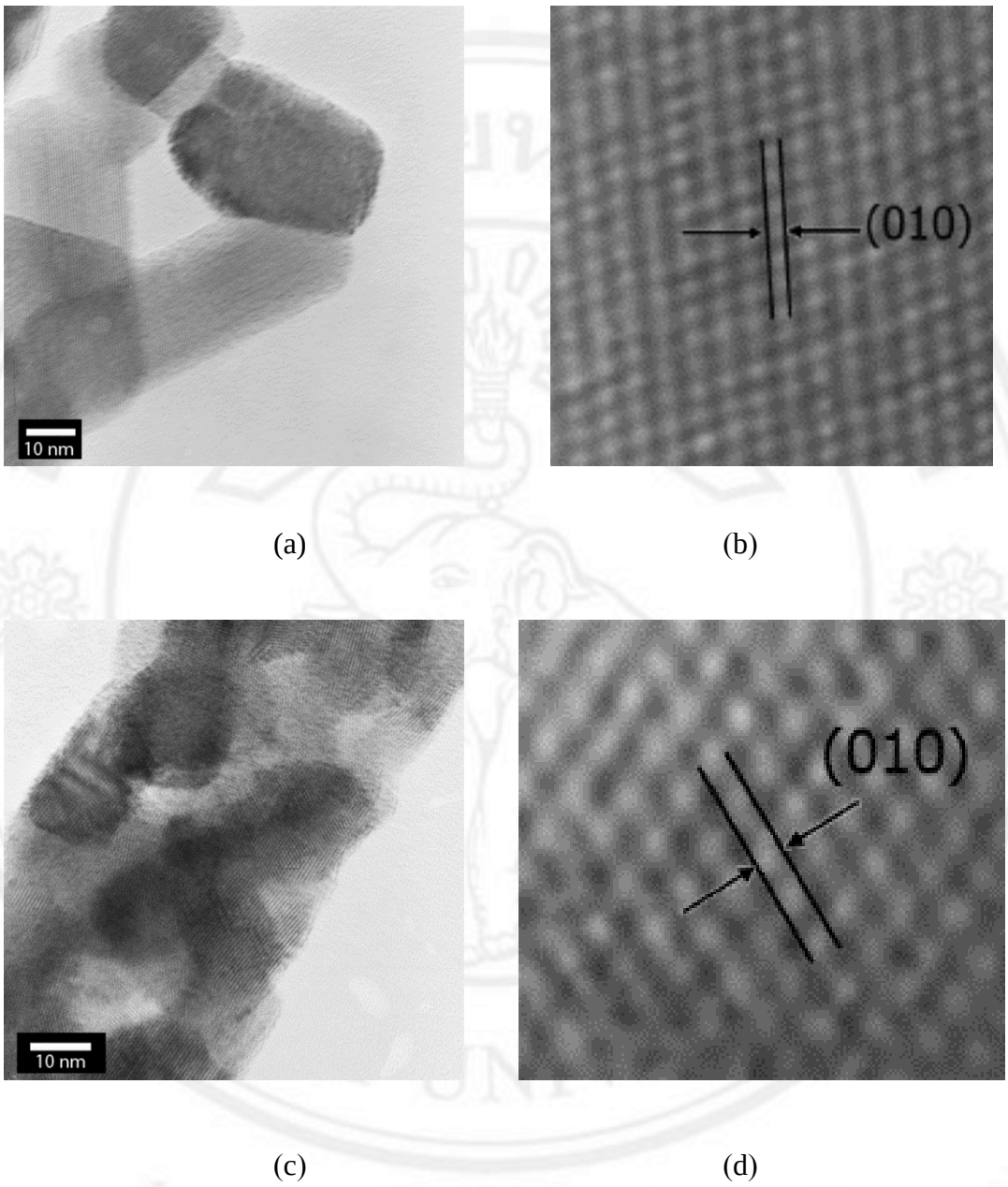

Figure 4.2.13 TEM and HRTEM images of the product prepared using 1.5 mmol $(CH_3COO)_2$ Mg·$4H_2O$, $(NH_4)_6W_7O_{24}$·$4H_2O$, and PVA 1.3 g, as starting reagents and calcination at 500 ^oC for 3 h (a and b), (c and e) of the product prepared using 4.5 mmol $(CH_3COO)_2$ Mg·$4H_2O$, $(NH_4)_6W_7O_{24}$·$4H_2O$, and PVA 1.3 g as starting reagents and calcination at 500 ^oC for 3 h.

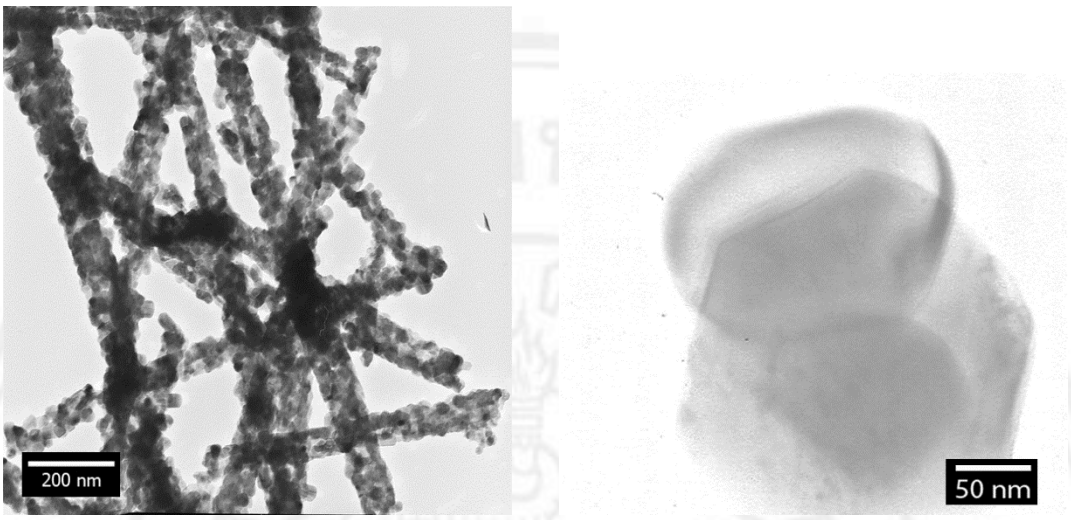

(a) (b)

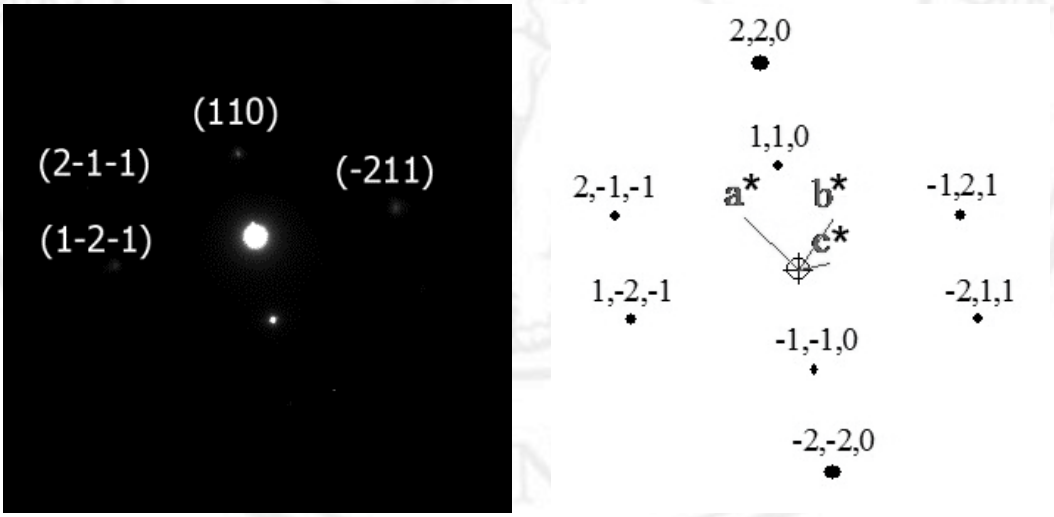

(c) (d)

Figure 4.2.14 TEM of the (a) product prepared using 1.5 mmol $(CH_3COO)_2$ $Mg{\cdot}4H_2O$, $(NH_4)_6W_7O_{24}{\cdot}4H_2O$, and PVA 1.3 g as starting reagents and calcination at 500 ^oC for 3 h . TEM, and SAED and simulated patterns of the (b-d) product prepared using 4.5 mmol $(CH_3COO)_2$ $Mg{\cdot}4H_2O$, $(NH_4)_6W_7O_{24}{\cdot}4H_2O$, and PVA 1.3 g, as starting reagents and calcination at 700 ^oC for 3 h.

PL spectra of $MgWO_4$, synthesized from the MW5 solution, after calcination at 500 ^oC, 600 ^oC and 700 ^oC for 3 h (Figure 4.2.15). In the present research, the emission peaks were in the spectral region at 446–479 nm having the potential applications for photonic sensors and devices. Starting from 500 ^oC to 700 ^oC calcination, PL intensities were increased with the increase in the calcination temperatures, and became the highest at 700 ^oC calcination.

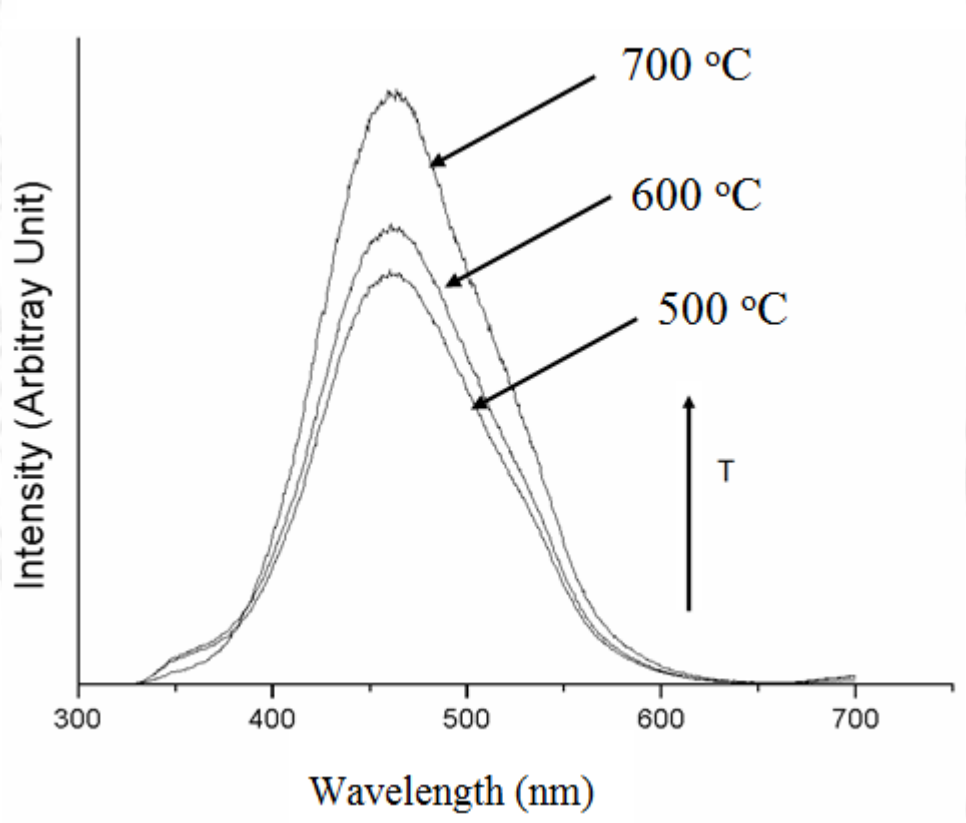

Figure 4.2.15 PL emission of the MW5C1, MW5C2 and MW5C3 products synthesized from the product prepared using 4.5 mmol $(CH_3COO)_2$ $Mg{\cdot}4H_2O$, $(NH_4)_6W_7O_{24}{\cdot}4H_2O$, and PVA 1.3 g as starting reagents, and calcination at 500 ^oC, 600 ^oC, and 700 ^oC for 3 h respectively.

UV–visible absorption (Figure 4.2.17 and Figure 4.2.18) of MW5C3 indicated an exponential decreasing of photonic absorption attenuated through the product. Its indirect Eg was determined, by extrapolating linear portion of the curve to zero absorption, to be 4.19 eV – very close to that reported by Lacomba-Perales et al. [118], and Kim et al. [119]. Particlesizes and morphologies could play the role in the absorbance characteristics [120,121], having the influence on the energy gap.

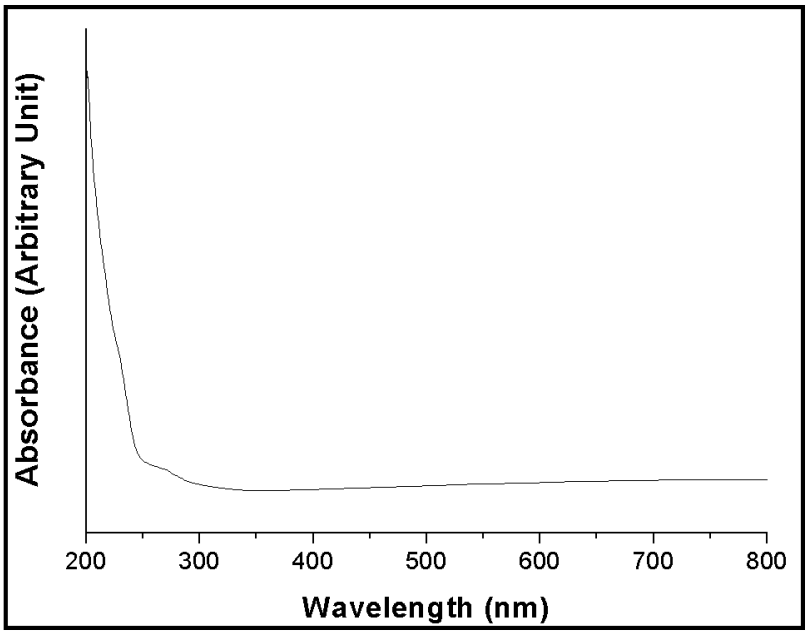

Figure 4.2.16 UV–visible absorption of the MW5C3, the product prepared using 4.5 mmol $(CH_3COO)_2$ Mg·$4H_2O$, $(NH_4)_6W_7O_{24}$·$4H_2O$, and PVA 1.3 g as starting reagents, and calcination at 700 ºC for 3 h.

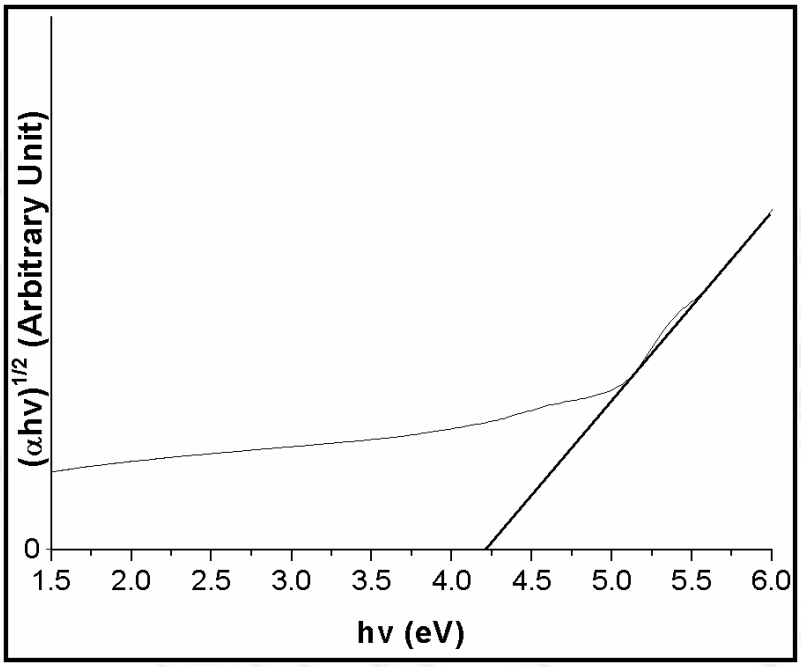

Figure 4.2.17 The $(\alpha h\nu)^{1/2}$ versus hν plot of the $MgWO_4$, synthesized from the MW5C3, the product prepared using 4.5 mmol $(CH_3COO)_2$ $Mg{\cdot}4H_2O$, $(NH_4)_6W_7O_{24}{\cdot}4H_2O$, and PVA 1.3 g as starting reagents, and calcination at 700 ^oC for 3 h.

4.3 $MgMoO_4$ synthesized by electrospinning method

Figure 4.3.1 compares TGA curve of the MM3 spider's web to that of PVA. The weight loss of PVA (Figure 4.3.1) exhibited the degradation process for three steps: 10.5 wt% due to the evaporation of loosely bound water at 32–200 ^oC, 79.3 wt% predominantly caused by the decomposition of PVA structure at 200–420 ^oC, and 8.3 wt% by the breaking of PVA backbone at 420–490 ^oC. Its weight tended to be constant upon further heating above 490 ^oC [96]. For the M3 as spun fibrous web, it weight loss (Figure 4.3.1) was 33.5 wt% associated with water evaporation at 32–226 1C, 41.2 wt% caused by the decomposition of PVA at 226–420 ^oC, and 7.7 wt%

seemed to be the oxidation and decomposition of the PVA main chain at 420–519 ºC. These last two steps were attributed to the loss of PVA and organic compound blended in the fibrous web. Above 519 ºC, there was no significant change in its weight.

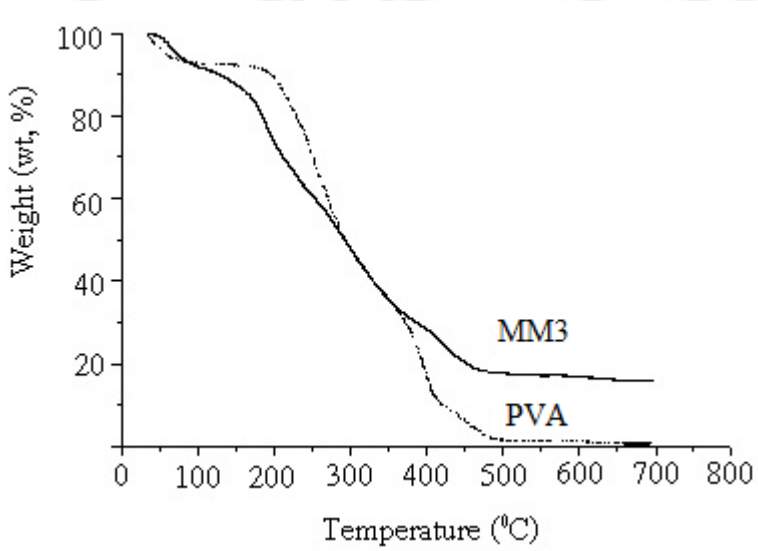

Figure 4.3.1 TGA curves of PVA and the $MgMoO_4$-PVA, synthesized from the 4.5 mmol $(CH_3COO)_2Mg{\cdot}4H_2O$, $(NH_4)_6Mo_7O_{24}{\cdot}4H_2O$, and PVA 1.3 g as starting reagents.

XRD spectra (Figure 4.3.2) of the MM3 fibrous webs after calcination at 400, 500 and 600 ºC for 3 h corresponded to the monoclinic structured $MgMoO_4$ and C2/m space group (JCPDS database no. 01-072-2153) [94]. The temperatures played a role in the crystalline degree and purity of the $MgMoO_4$ fibrous webs. At 400 ºC, the fibrous web was not perfectly pure $MgMoO_4$, containing some residual PVA at 2Θ of approximately 22.5º [98], and graphite (JCPDS database no. 00-001-0640) at 2Θ = 26.3º of the (002) crystallographic plane [100]. Upon increasing the calcination temperatures to 500 and 600 ºC, the spectra became sharper and the XRD intensities

were stronger. The crystalline degree of the fibrous webs was considerably improved. No PVA and graphite were detected. At 600 ^{o}C calcination, the fibrous web was the best pure crystal. Its crystalline degree was the highest, and the atoms resided in the perfect crystal lattice. By using the Scherrer formula [122], crystallite sizes of the MM3 fibrous webs after 400, 500 and 600 ^{o}C calcination for 3 h were 23.1, 25.9, and 52.0 nm, respectively. PVA and organic compound blended in the fibrous web.

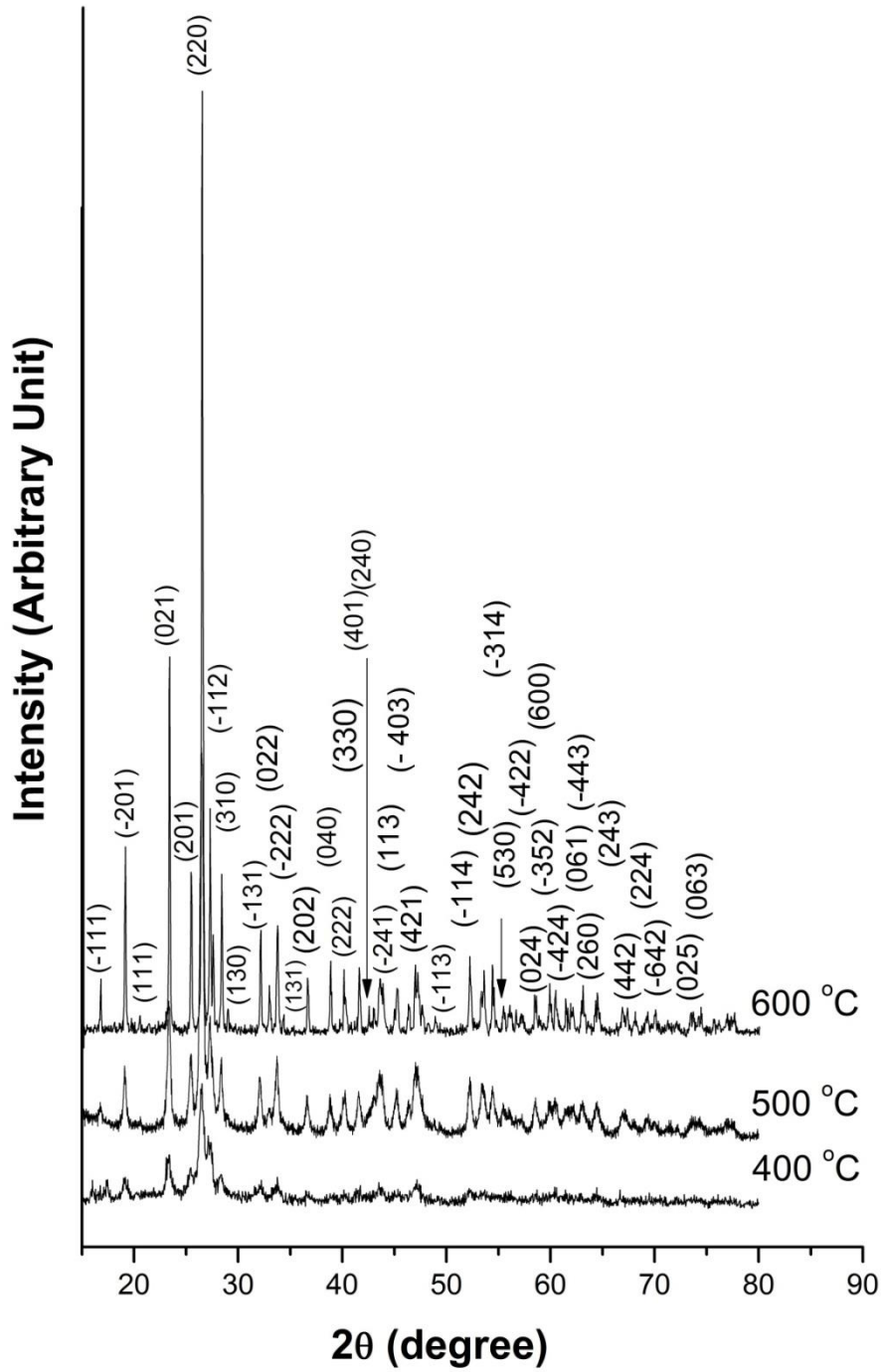

Figure 4.3.2 XRD spectra of the $MgMoO_4$ fibrous webs, synthesized from the 4.5 mmol $(CH_3COO)_2Mg{\cdot}4H_2O$, $(NH_4)_6Mo_7O_{24}{\cdot}4H_2O$, and PVA 1.3 g as starting reagents and calcination at 500 ^oC, 600 ^oC , and 700 ^oC for 3 h respectively.

SEM images (Figure 4.3.3-4.3.5) of the as-spun products of the MM1, MM2, and MM3 mixtures were composed of fibers and electrospun like spiders' webs with smooth surfaces. Some beads were also detected on the MM1 and MM2 fibrous webs, controlled by viscosity and density of the mixtures. When the content of PVA was as high as 1.3 g, the beads were no longer detected. It was exactly right to eject the mixture with sufficiently high viscosity and density out of the hollow needle to form the bead-free web. In the present research, the $MgMoO_4$ nuclei blended in the fibrous webs were invisible. When the MM3 fibrous webs were calcined at 400, 500 and 600 ^oC for 3 h, the fibers were thinned—caused by the evaporation of PVA and volatile components. The $MgMoO_4$ nuclei also grew up to be nanoparticles. At 400 ^oC and 3 h calcination, the fibrous surface (Figure 4.3.6) was smooth, showing that some PVA coating remained on the surface. Upon increasing the calcination temperatures from 400 ^oC to 500 ^oC and 600 ^oC (Figure 4.3.6-4.3.8), their surfaces became roughened. At 600 ^oC and 3 h calcination, the fibers were of 50–100 nm diameters, and were composed of 20–50 nm nanoparticles.

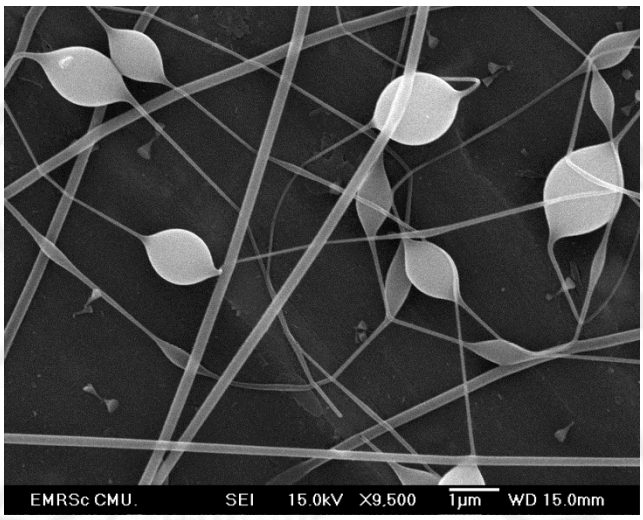

Figure 4.3.3 SEM image of the product prepared using 4.5 mmol $(CH_3COO)_2Mg{\cdot}4H_2O$, $(NH_4)_6Mo_7O_{24}{\cdot}4H_2O$, and PVA 0.7 g as starting reagents (Sample code MM1).

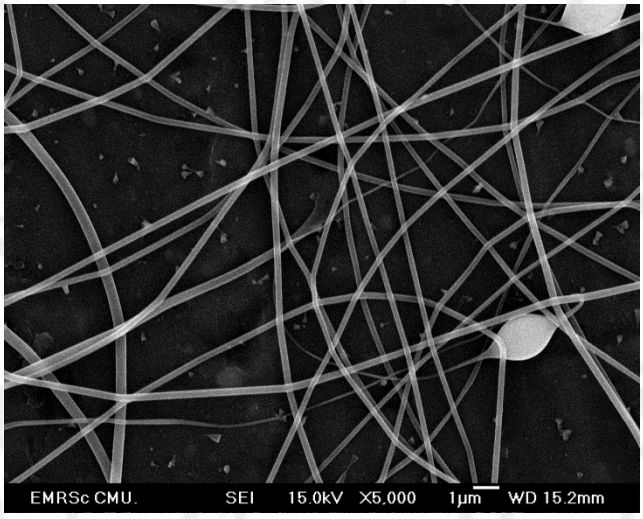

Figure 4.3.4 SEM image of the product prepared using 4.5 mmol $(CH_3COO)_2Mg{\cdot}4H_2O$, $(NH_4)_6Mo_7O_{24}{\cdot}4H_2O$, and PVA 1.0 g as starting reagents (Sample code MM2).

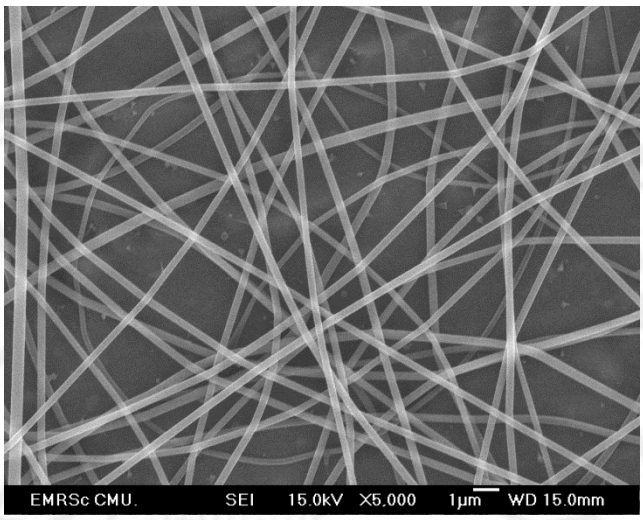

Figure 4.3.5 SEM image of the product prepared using 4.5 mmol $(CH_3COO)_2Mg{\cdot}4H_2O$, $(NH_4)_6Mo_7O_{24}{\cdot}4H_2O$, and PVA 1.3 g as starting reagents (Sample code MM3).

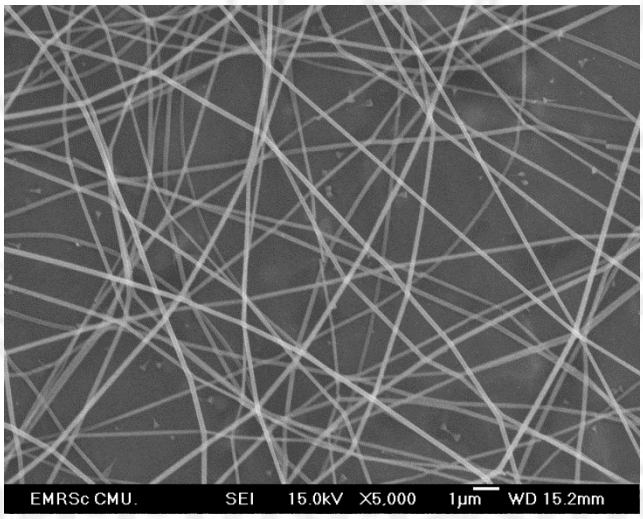

Figure 4.3.6 SEM image of the product prepared using 4.5 mmol $(CH_3COO)_2Mg{\cdot}4H_2O$, $(NH_4)_6Mo_7O_{24}{\cdot}4H_2O$, and PVA 1.3 g as starting reagents and calcination at 400 ^oC for 3 h (Sample code MM3C1).

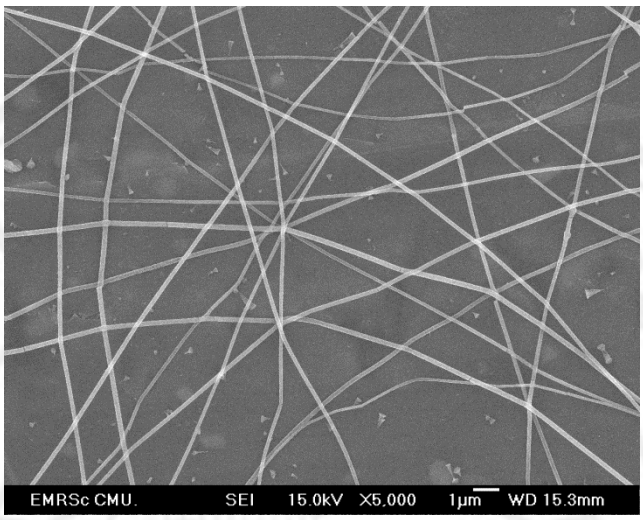

Figure 4.3.7 SEM image of the product prepared using 4.5 mmol $(CH_3COO)_2Mg{\cdot}4H_2O$, $(NH_4)_6Mo_7O_{24}{\cdot}4H_2O$, and PVA 1.3 g as starting reagents and calcination at 500 ºC for 3 h (Sample code MM3C2).

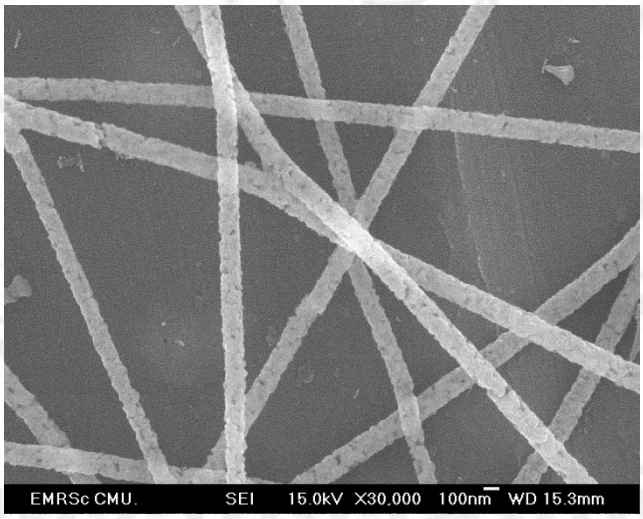

Figure 4.3.8 SEM image of the product prepared using 4.5 mmol $(CH_3COO)_2Mg{\cdot}4H_2O$, $(NH_4)_6Mo_7O_{24}{\cdot}4H_2O$, and PVA 1.3 g, as starting reagents and calcination at 600 ºC for 3 h (Sample code MM3C3).

TEM images, HRTEM and SAED patterns (Figure 4.3.9 and Figure 4.3.10) of the products with 500 ^{o}C and 600 ^{o}C calcinations. The number of (021) and (-111) crystallographic planes of typical nanoparticles (Figure 4.3.9 and Figure 4.3.10 d) with 500 ^{o}C and 600 ^{o}C calcination for 3 h were detected by HRTEM. SAED patterns were interpreted [94], and specified at the (042), (021), and (031) planes (Figure 4.3.10 a) with electron beam [$\bar{1}\bar{1}1$] direction. Comparing between the corresponding interpreted and simulated patterns, they are in good accordance.

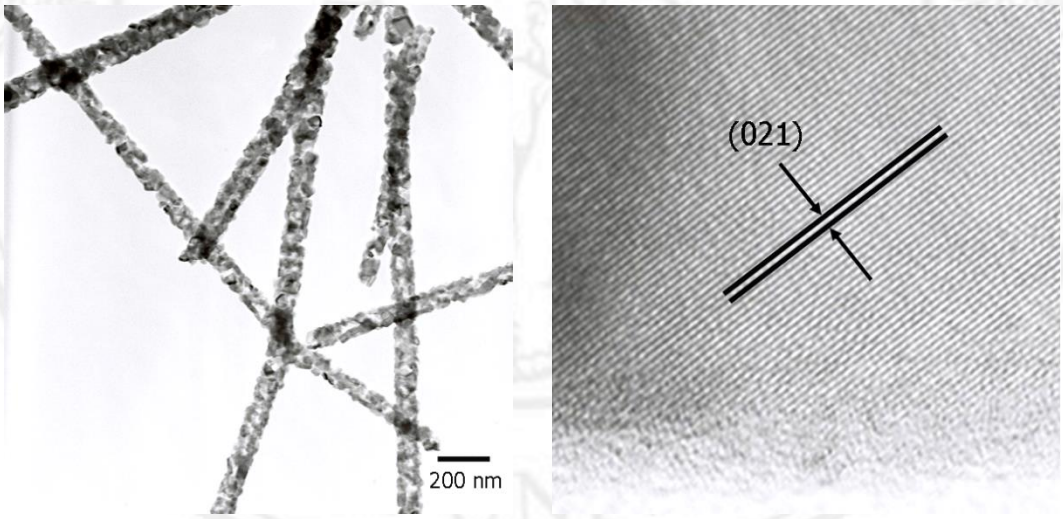

(a) (b)

Figure 4.3.9 TEM and HRTEM images of the MM3 fibrous webs, the product prepared using 4.5 mmol $(CH_3COO)_2$ Mg·$4H_2O$, $(NH_4)_6Mo_7O_{24}$·$4H_2O$, and PVA 1.3 g as starting reagents reagents, after calcination at (a and b) 500 ^{o}C for 3 h.

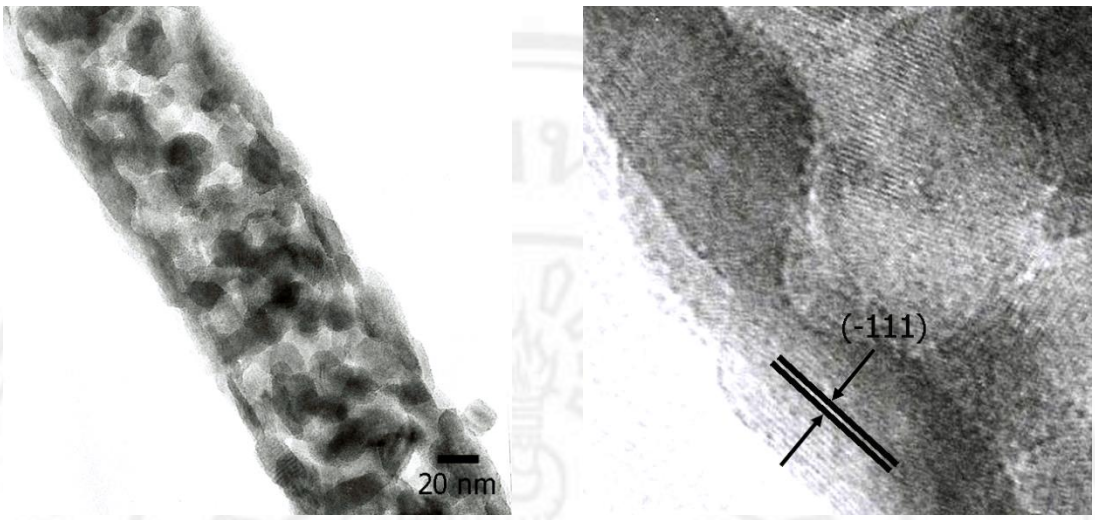

(a) (b)

Figure 4.3.10 TEM and HRTEM images of the MM3 fibrous webs, the product prepared using 4.5 mmol $(CH_3COO)_2$ Mg·$4H_2O$, $(NH_4)_6Mo_7O_{24}$·$4H_2O$, and PVA 1.3 g as starting reagents, after calcination at (a and b) 600 ^oC for 3 h.

Figure 4.3.11 shows FTIR spectra of PVA and the MM3 fibrous webs before and after calcination at 400, 500 and 600 ^oC for 3 h. obviously, the major vibrational modes associated with PVA were the following. The O–H stretching of alcohol and residual water was detected at 3600–3200 cm^{-1}. The vibrational mode at 2943 cm^{-1} corresponds to the C–H stretching of alkyl groups. The C=O stretching mode was detected at 1721 cm^{-1}, CH_2 bending mode at 1448 cm^{-1}, and C–O stretching mode of carboxyl at 1098 cm^{-1} [123,124]. When the MM3 as-spun fibrous web was characterized by FTIR, additional four asymmetric stretching modes of Mo–O–Mo were detected at 970, 893, 835, and 736 cm^{-1} [125], and bending mode of Mo–O at 427 cm^{-1}. Once, the MM3 as-spun fibrous webs were calcined at 400, 500 and 600 ^oC for 3 h, the PVA evaporated and decomposed. At higher temperatures, the vibrational

modes of PVA became weakened, and those of $MgMoO_4$ were stronger until at 500 and 600 ^oC and 3 h calcination, where the vibrations of PVA were no longer detected. The vibrations of $MgMoO_4$ were the strongest at 600 ^oC and 3 h calcination.

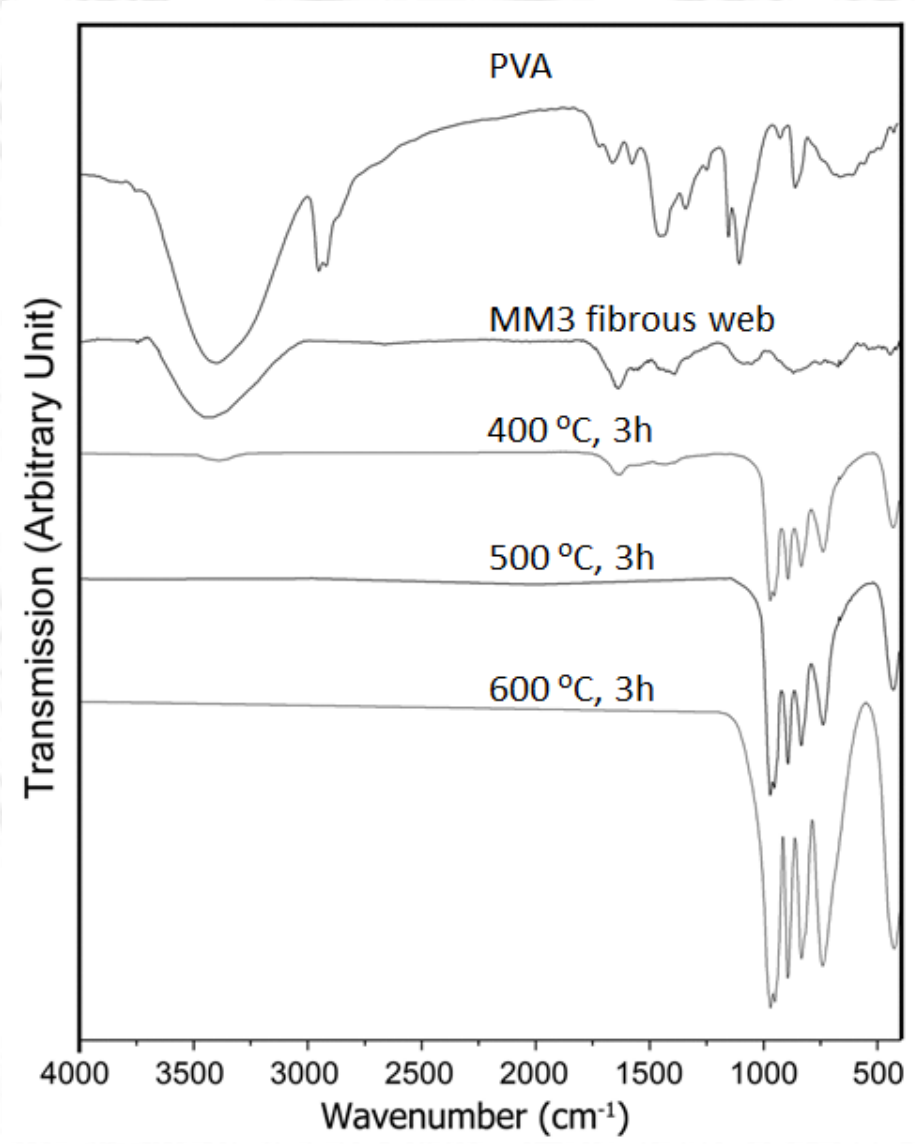

Figure 4.3.11 FTIR spectra of PVA and the MM3 fibrous webs, the product prepared using 4.5 mmol $(CH_3COO)_2$ $Mg{\cdot}4H_2O$, $(NH_4)_6Mo_7O_{24}{\cdot}4H_2O$, and PVA 1.3 g as starting reagents, before and after calcination at 400, 500 and 600 ^oC for 3 h, respectively.

Raman spectrum of the MMC3 fibrous web with 600 ºC and 3h calcination is shown in Fig.4.3.12 The strong peaks at 962 and 949 cm^{-1} were assigned to the $\nu_1(A_g)$ symmetric stretching modes. Those at 904, 870, and 848 cm^{-1} belonged to the ν_3 (A_g/B_g) modes, which were similar to the two split triply degenerate ν_3 modes. The splitting could be as large as 150 cm^{-1}. Comparing the ν_1 and ν_3 vibration modes, the first have stronger intensities and higher frequencies (wavenumbers) than those of the second. The Raman shifts at 423, 386, 370, 335 and 279 cm^{-1} were unable to be specifically identified among the two ν_2 and ν_4 bending and lattice vibration modes equal in intensities, due to the strong interaction between the tetrahedrons and the coupling with the Mg–O stretching modes. The remaining ones at 205, 177, and 156 cm^{-1} corresponded to the lattice vibrations of A_g/B_g modes [126].

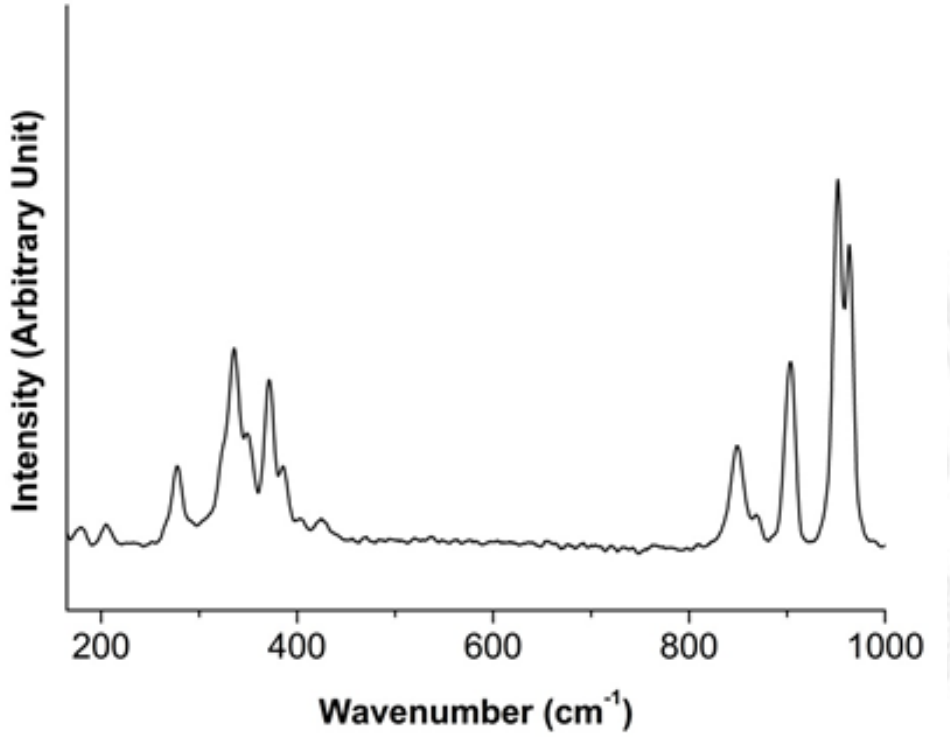

Figure 4.3.12 Raman spectrum of the MMC3 fibrous web, the product prepared using 4.5 mmol $(CH_3COO)_2$ Mg·$4H_2O$, $(NH_4)_6Mo_7O_{24}$·$4H_2O$, and PVA 1.3 g as starting reagents, after calcination at 600 ^oC for 3 h.

UV–visible absorption of the MMC3 fibrous web with 600 ^oC and 3 h calcination is shown in Figure 4.3.13. For photon energy (hn) greater than energy gap (Eg), the relationship between the square absorbance and the hn for direct interband transitions was linearly increased with the increasing of hn [127]. Its direct energy gap was 5.15 eV, due to the absorption spectrum in the vicinity of the fundamental absorption edge, caused by the electronic transition in the $(MoO_4)^{-2}$ complex. This energy gap is in accordance with that reported by Spasskii et al. [21]. Particle sizes and morphologies were found to play a role in the absorbance characteristics [120], which have an influence on the energy gap as well.

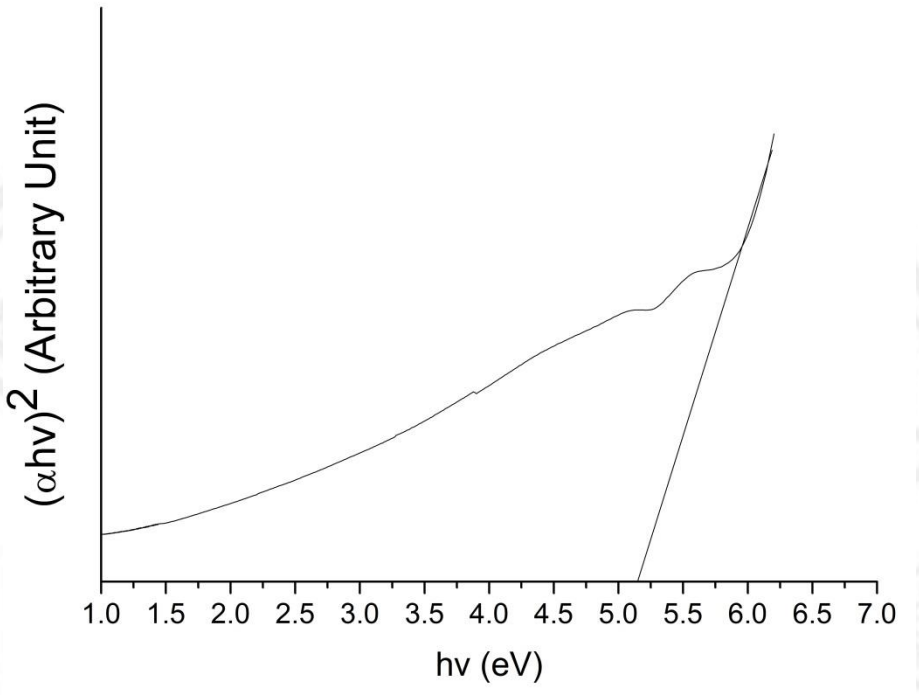

Figure 4.3.13 UV-visible absorption of the MMC3 fibrous web, the product prepared using 4.5 mmol $(CH_3COO)_2$ $Mg{\cdot}4H_2O$, $(NH_4)_6Mo_7O_{24}{\cdot}4H_2O$, and PVA 1.3 g as starting reagents, after calcination at 600 ºC for 3 h.

4.4 $SrMoO_4$ synthesized by microwave-hydrothermal method

Comparing XRD patterns (Figure 4.4.1- 4.4.3) to the JCPDS no. 01-085-0586 [61]. They were specified as primitive tetragonal scheelite structured $SrMoO_4$ [79,129,130]. No other characteristic peaks of impurities were detected. The Sr^{2+} cations were mixed with $[Mo_7O_{24}]^{6-}$ anions to form intermediate complexes at room temperature. Upon processing the complexes by the microwave-hydrothermal combination, they were gradually transformed for a few steps into $SrMoO_4$ precipitates. The XRD peaks became sharpened with the increase in the length of

time, including the crystalline degree was much improved and the crystals were enlarged. The longer processing time was used, the larger crystallite size and the better crystalline degree would be. Calculated crystallite sizes of the MSA3, MSB3 and MSC3 products [100] were 34.7, 64.7 and 83.2 nm, respectively. They seemed to be influenced by different intermediates, which led to form crystals with different sizes.

XRD peaks (Figure 4.4.1) of the purified $SrMoO_4$ produced in the solution containing $Sr(NO_3)_2$ and $(NH_4)_6Mo_7O_{24}{\cdot}4H_2O$ by the microwave-hydrothermal reaction for 30 min were compared with that obtained by simulation [111]. The 2θ Bragg angles and peak intensities obtained from the experiment, simulation and JCPDS database were in good accordance. Crystal growth rates along the x-, y- and z-directions could be different. The simulated scheelite-type tetragonal structured $SrMoO_4$ (Figure 4.4.4) belongs to $I4_1/a$ space group with two $SrMoO_4$ formula units with inversion centers per primitive unit cell. The Sr and Mo sites have S_4 point symmetry. The O sites have only a little symmetry and reside as almost tetrahedral coordination surrounding each of the Mo sites, composing as $[MoO_4]^{2-}$ tetrahedral configuration. Each Sr atom shares corners with eight adjacent O atoms of $[MoO_4]^{2-}$ tetrahedrons. $Sr^{\alpha+}$ cations form bond with $[MoO_4]^{\alpha-}$ anions to produce $SrMoO_4$ crystal structure with $\alpha \rightarrow 2$, including the $[MoO_4]^{2-}$ units with strong Mo–O covalent bonds [19, 27, 130].

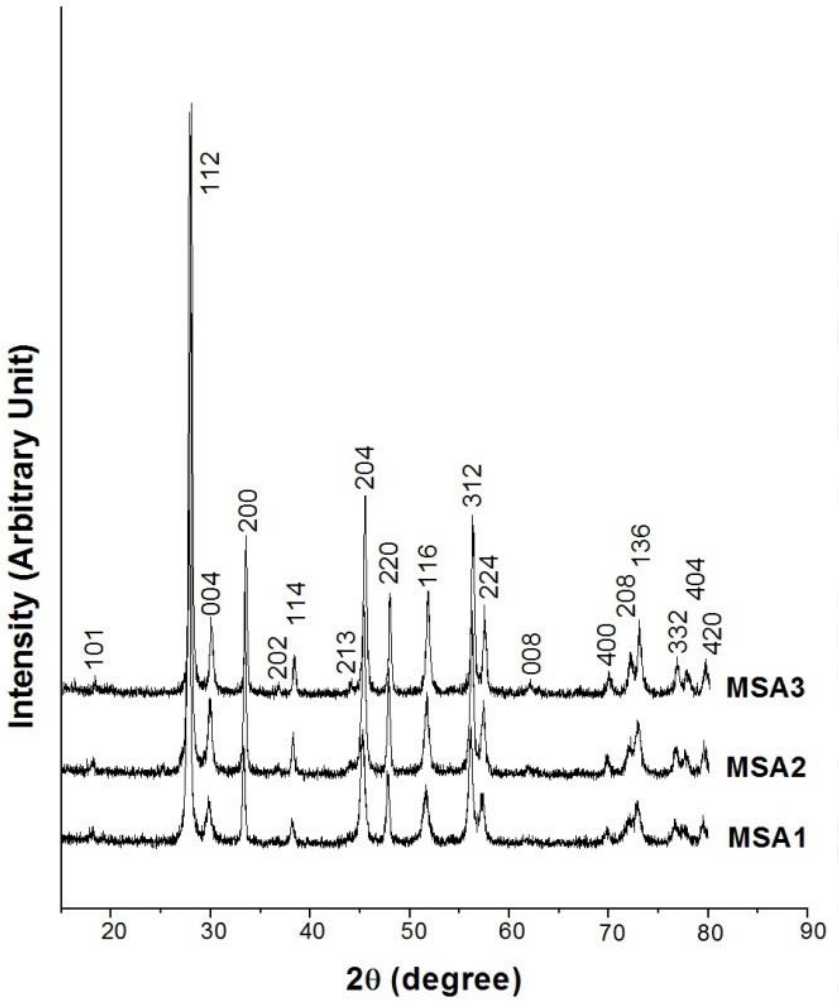

Figure 4.4.1 XRD patterns of (a) MSA1, MSA2 and MSA3, the product prepared using 5.0 mmol $Sr(NO_3)_2$, and $(NH_4)_6Mo_7O_{24}{\cdot}4H_2O$ as starting reagents and a 270 w microwave-hydrothermal for 5, 15, and 30 min respectively.

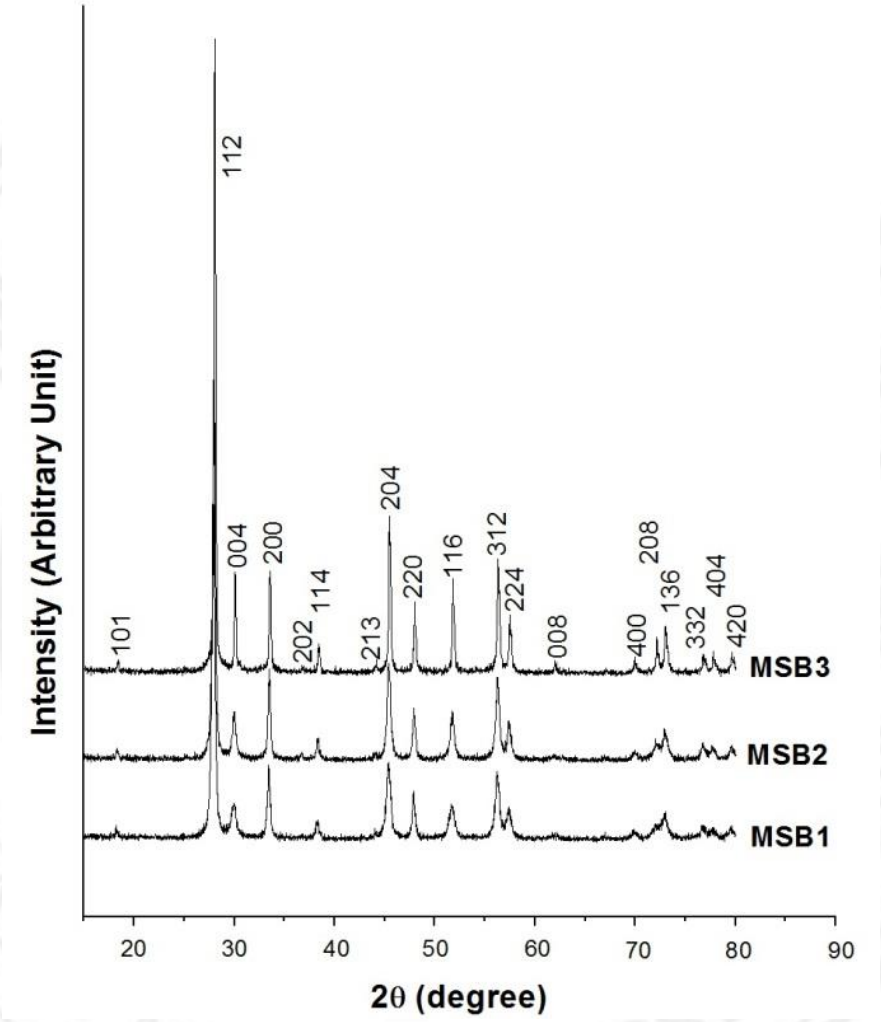

Figure 4.4.2 XRD patterns of MSB1, MSB2 and MSB3, of the product prepared using 5.0 mmol $Sr(CH_3CO_2)_2$, and $(NH_4)_6Mo_7O_{24}{\cdot}4H_2O$ as starting reagents and a 270 w microwave-hydrothermal for 5, 15, and 30 min respectively.

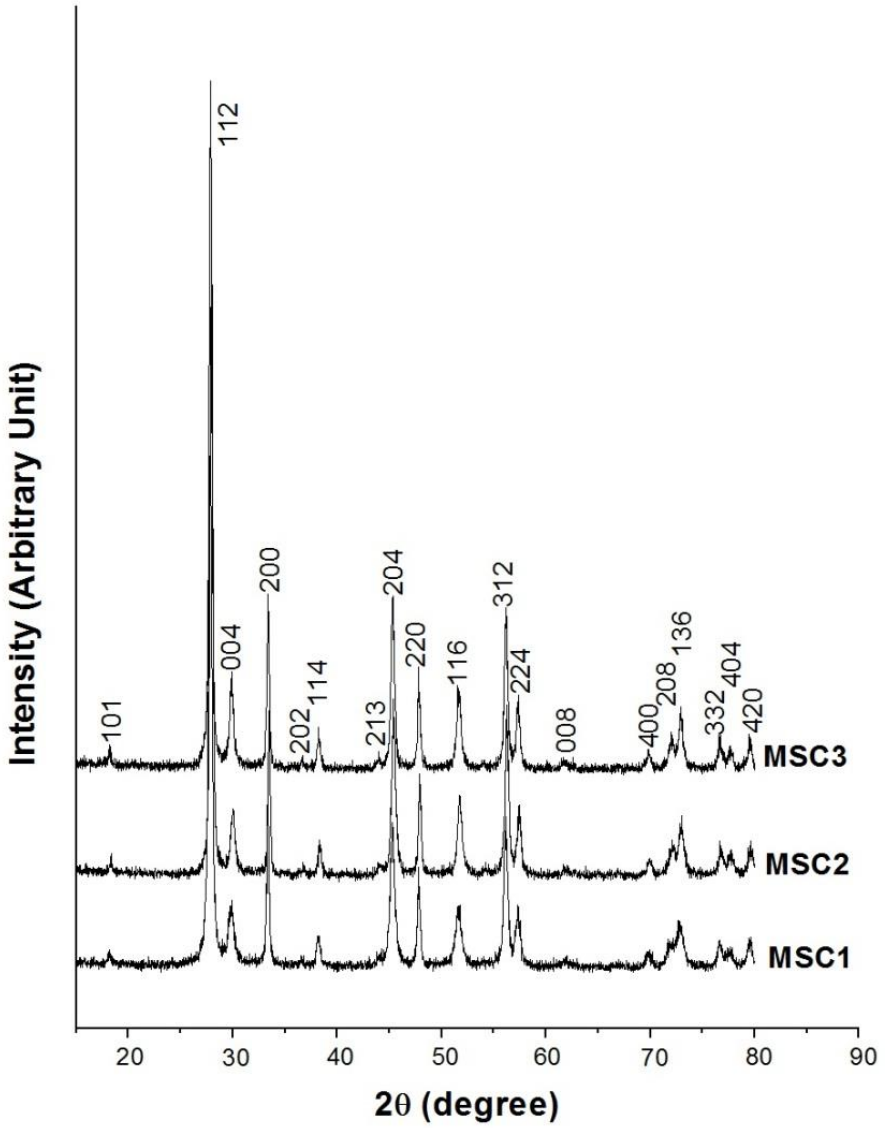

Figure 4.4.3 XRD patterns of MSC1, MSC2 and MSC3, the product prepared using 5.0 mmol $SrCl_2 \cdot 6H_2O$, and $(NH_4)_6Mo_7O_{24} \cdot 4H_2O$ as starting reagents and a 270 w microwave-hydrothermal for 5, 15, and 30 min respectively.

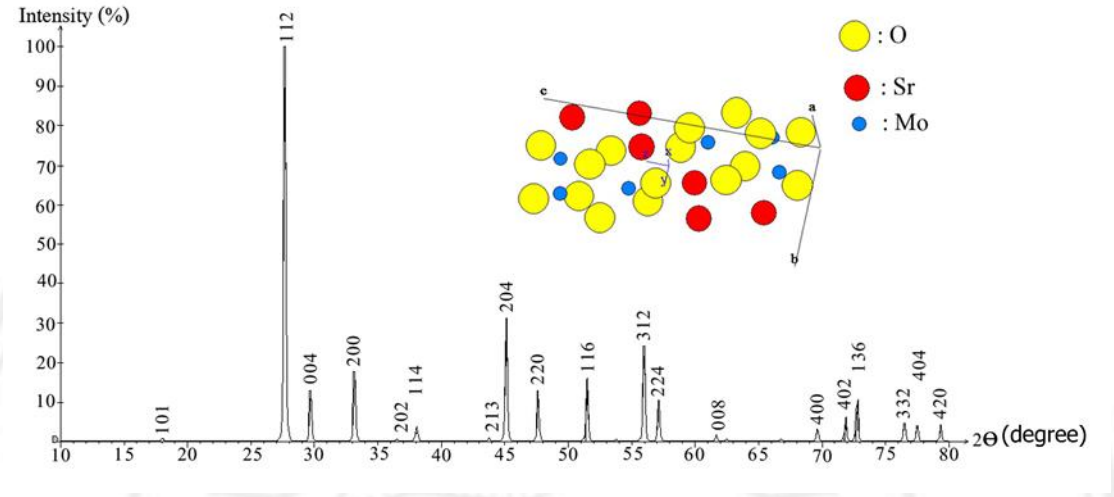

Figure 4.4.4 Simulated XRD pattern and crystal structure of $SrMoO_4$, the product prepared using 5.0 mmol $Sr(NO_3)_2$, and $(NH_4)_6Mo_7O_{24}\cdot 4H_2O$ as starting reagents and a 270 w microwave-hydrothermal for 30 min.

SEM images (Figure 4.4.5 - Figure 4.4.17) show examples of the hierarchical architectures of $SrMoO_4$ produced using different strontium precursor and $(NH_4)_6Mo_7O_{24}\cdot 4H_2O$ by microwave-hydrothermal reactions for different lengths of time. The hierarchical architectures with donut-like or flower-like shape were composed of a number of $SrMoO_4$ nanosheets with 2-3 nm thick for the products produced using $Sr(NO_3)_2$ or $SrCl_2\cdot 6H_2O$ and $(NH_4)_6Mo_7O24\cdot 4H_2O$, and of $SrMoO_4$ nanorods with 100-150 nm long for the product produced using $Sr(CH_3CO_2)_2$ and $(NH_4)_6Mo_7O_{24}\cdot 4H_2O$. Different morphologies seemed to be obtained from different intermediate complexes, influenced by different anions of Sr salts. They were continuously enlarged and densely populated and their sizes were increased with the increase of the processing time. At these stages, the nanosheets and nanorods were squeezed and their shapes were loose of symmetry, due to the stress developed inside.

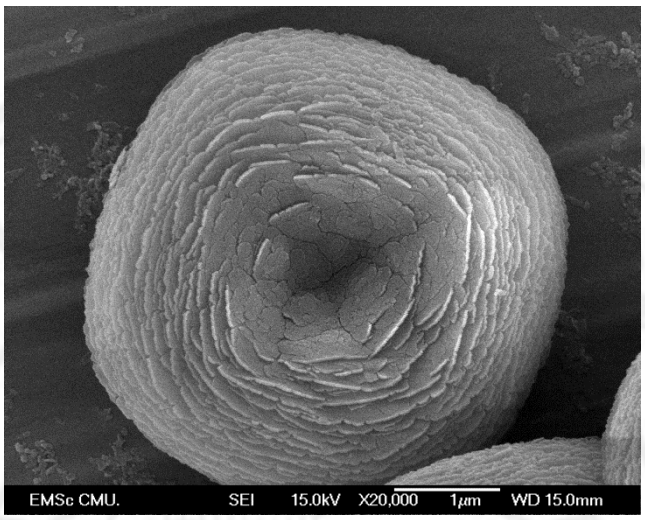

Figure 4.4.5 SEM image of the product prepared using 5.0 mmol $Sr(NO_3)_2$, $(NH_4)_6Mo_7O_{24}\cdot 4H_2O$ as starting reagents and a 270 w microwave-hydrothermal for 5 min (Sample code MSA1).

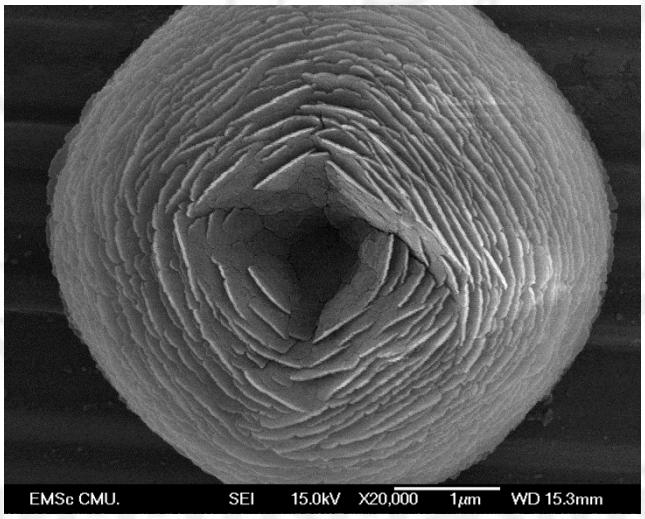

Figure 4.4.6 SEM image of the product prepared using 5.0 mmol $Sr(NO_3)_2$, $(NH_4)_6Mo_7O_{24}\cdot 4H_2O$ as starting reagents and a 270 w microwave-hydrothermal for 15 min (Sample code MSA2).

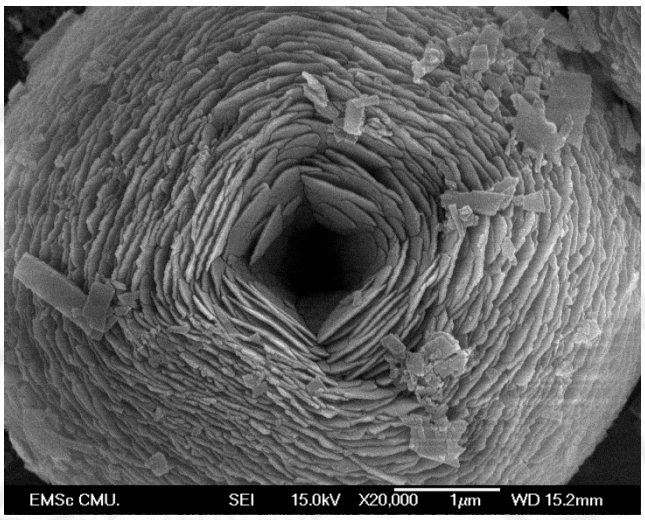

Figure 4.4.7 SEM image of the product prepared using 5.0 mmol $Sr(NO_3)_2$, $(NH_4)_6Mo_7O_{24}\cdot 4H_2O$ as starting reagents and a 270 w microwave-hydrothermal for 30 min (Sample code MSA3).

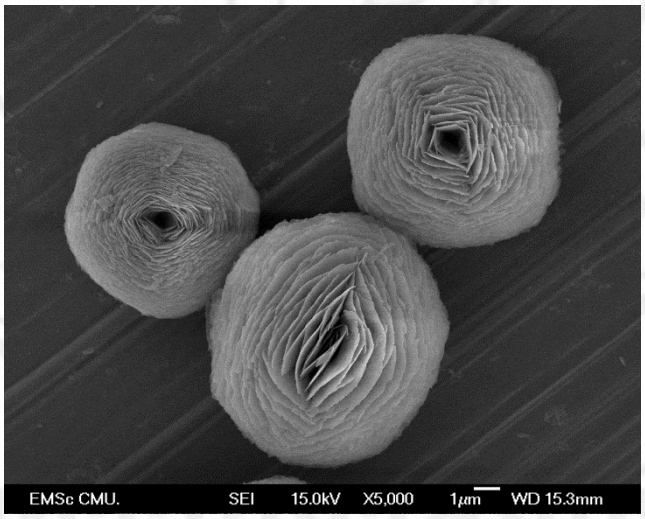

Figure 4.4.8 SEM image of the product prepared using 5.0 mmol $Sr(NO_3)_2$, $(NH_4)_6Mo_7O_{24}\cdot 4H_2O$ as starting reagents and a 270 w microwave-hydrothermal for 90 min (Sample code MSA4).

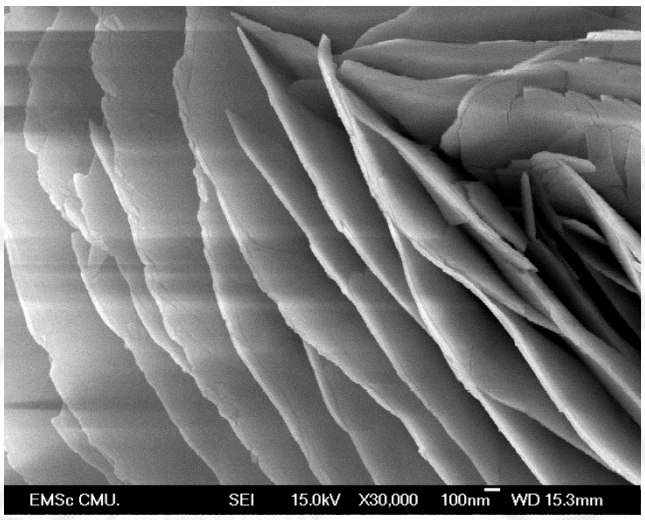

Figure 4.4.9 SEM image of the product prepared using 5.0 mmol $Sr(NO_3)_2$, $(NH_4)_6Mo_7O_{24}\cdot 4H_2O$ as starting reagents and a 270 w microwave-hydrothermal for 90 min (Sample code MSA4).

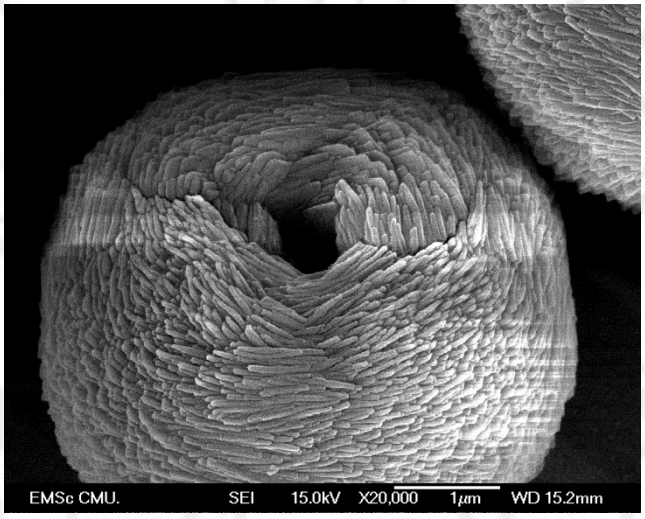

Figure 4.4.10 SEM image of the product prepared using 5.0 mmol $Sr(CH_3CO_2)_2$, $(NH_4)_6Mo_7O_{24}\cdot 4H_2O$ as starting reagents and a 270 w microwave-hydrothermal for 5 min (Sample code MSB1).

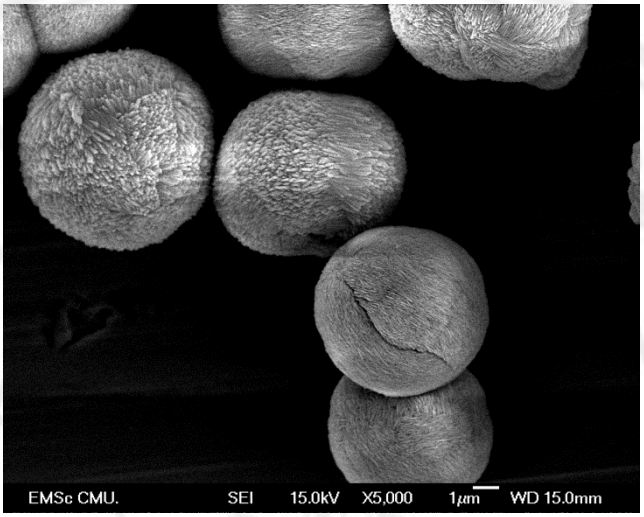

Figure 4.4.11 SEM image of the product prepared using 5.0 mmol $Sr(CH_3CO_2)_2$, $(NH_4)_6Mo_7O_{24}\cdot 4H_2O$ as starting reagents and a 270 w microwave-hydrothermal for 15 min (Sample code MSB2).

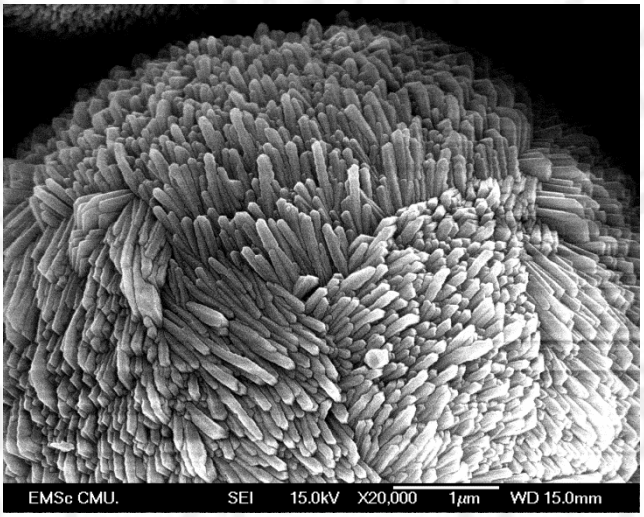

Figure 4.4.12 SEM image of the product prepared using 5.0 mmol $Sr(CH_3CO_2)_2$, $(NH_4)_6Mo_7O_{24}\cdot 4H_2O$ as starting reagents and a 270 w microwave-hydrothermal for 15 min (Sample code MSB2).

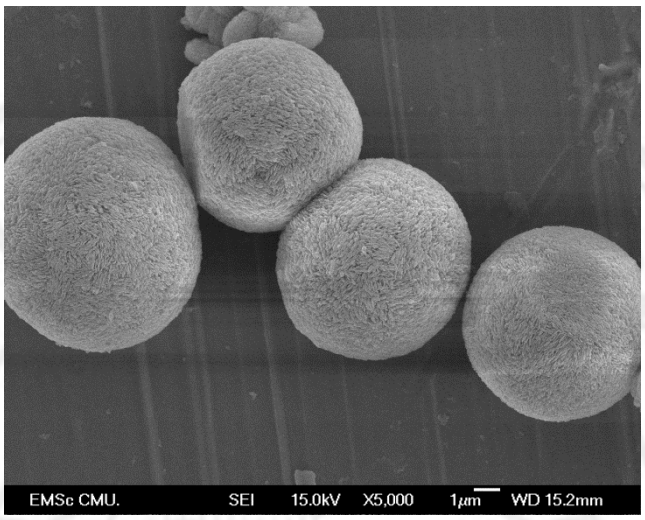

Figure 4.4.13 SEM image of the product prepared using 5.0 mmol $Sr(CH_3CO_2)_2$, $(NH_4)_6Mo_7O_{24}\cdot 4H_2O$ as starting reagents and a 270 w microwave-hydrothermal for 30 min (Sample code MSB3).

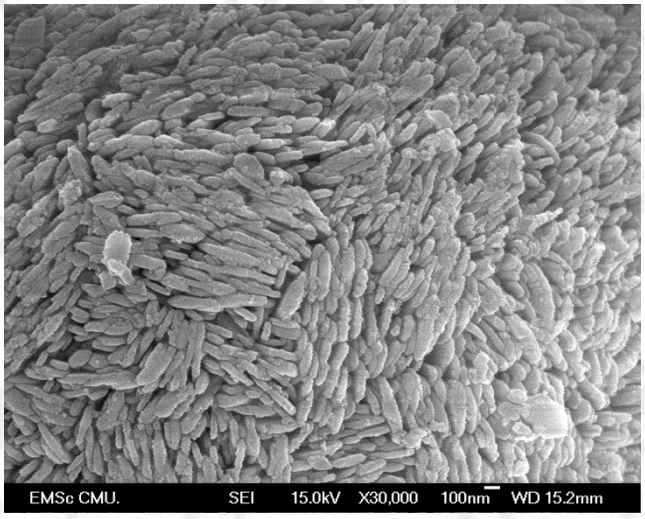

Figure 4.4.14 SEM image of the product prepared using 5.0 mmol $Sr(CH_3CO_2)_2$, $(NH_4)_6Mo_7O_{24}\cdot 4H_2O$ as starting reagents and a 270 w microwave-hydrothermal for 30 min (Sample code MSB3).

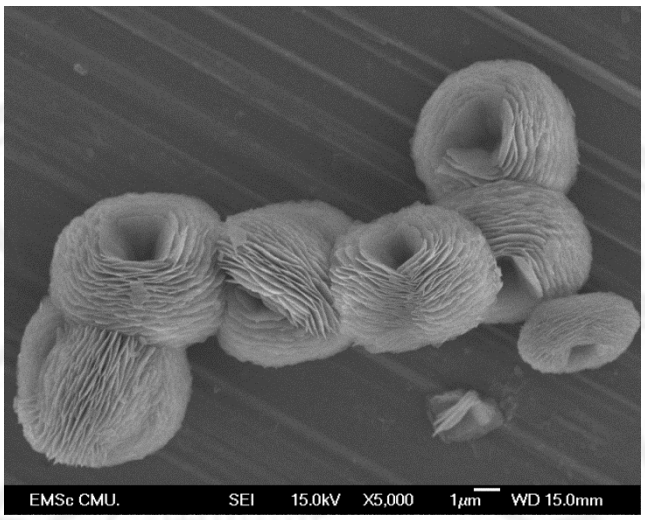

Figure 4.4.15 SEM image of the product prepared using 5.0 mmol $SrCl_2 \cdot 6H_2O$, $(NH_4)_6Mo_7O_{24} \cdot 4H_2O$ as starting reagents and a 270 w microwave-hydrothermal for 5 min (Sample code MSC1).

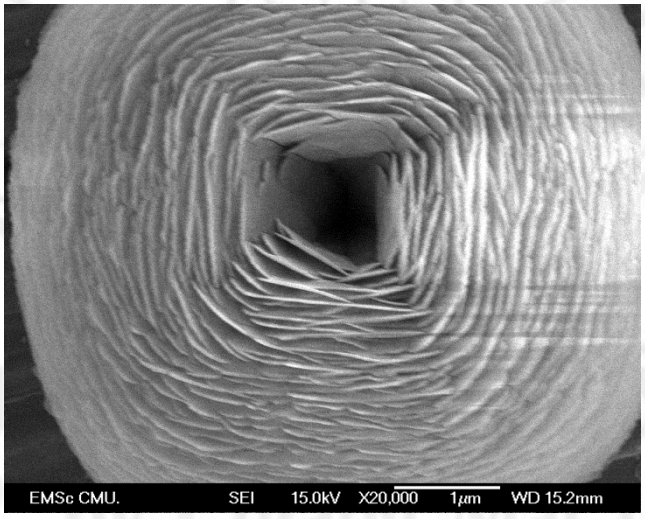

Figure 4.4.16 SEM image of the product prepared using 5.0 mmol $SrCl_2 \cdot 6H_2O$, $(NH_4)_6Mo_7O_{24} \cdot 4H_2O$ as starting reagents and a 270 w microwave-hydrothermal for 15 min (Sample code MSC2).

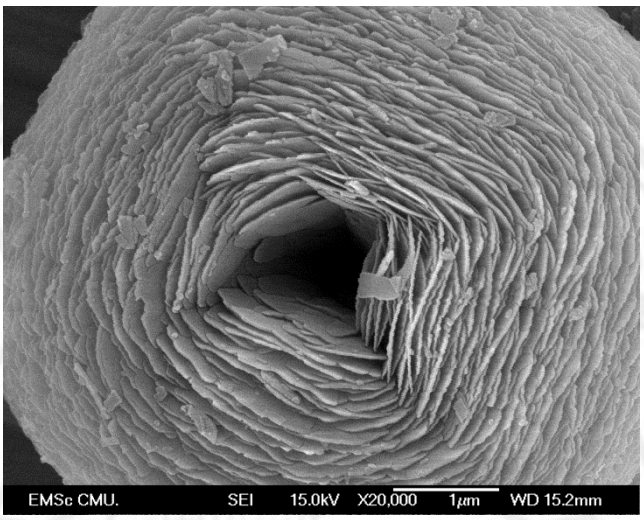

Figure 4.4.17 SEM image of the product prepared using 5.0 mmol $SrCl_2 \cdot 6H_2O$, $(NH_4)_6Mo_7O_{24} \cdot 4H_2O$ as starting reagents and a 270 w microwave-hydrothermal for 30 min (Sample code MSC3).

The donut-like product was confirmed by the TEM image (Figures 4.4.18 (a) and 4.4.18 (b)) of the MSA3 product, appeared as dark spherical area around the middle white one. A number of the (112) planes with 0.322 nm apart were detected. SAED diffraction pattern (Figure 4.4.18 (c)) with electron beam in the [0–10] direction belongs to the $SrMoO_4$ crystalline nanosheet. This interpreted pattern was in good accordance with the simulated one (Figure 4.4.18 (d)), although some spots of the simulated pattern did not appear on the interpreted one. To simulate the pattern, intensity and size of the spots (planes) were mutually related. The stronger intensity was used, the larger size was achieved. The intensity and size of the spots were limited by a saturated intensity used for simulation. Thus the spots of the simulated pattern with low intensity were absent from the interpreted one.

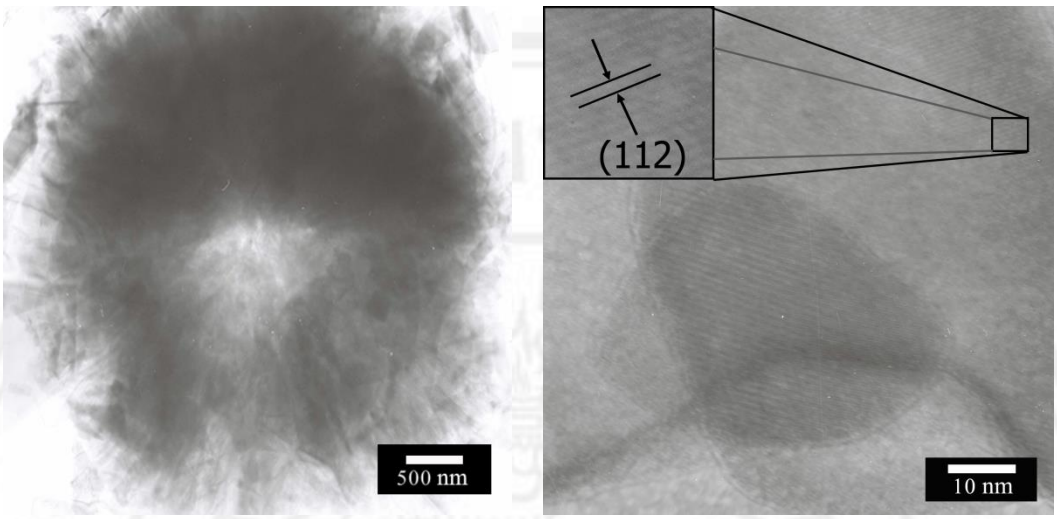

(a) (b)

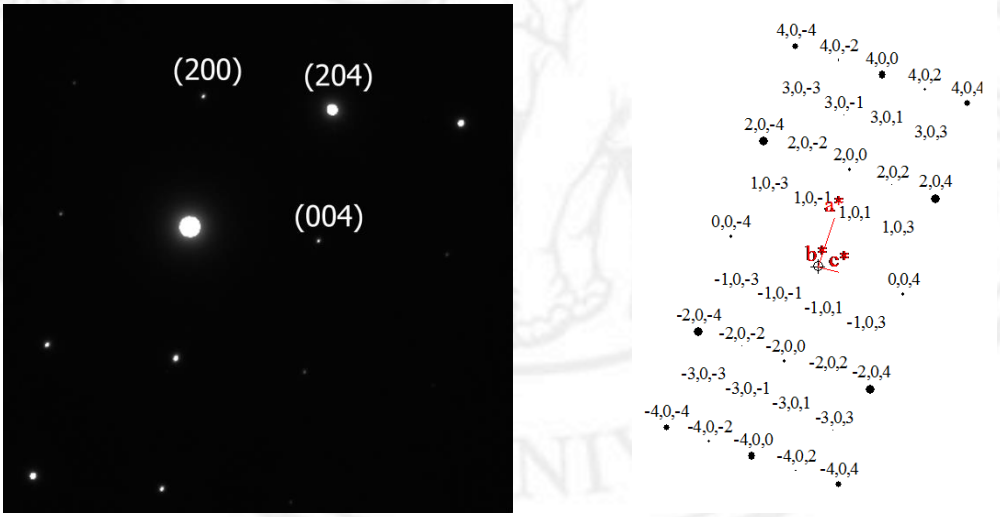

(c) (d)

Figure 4.4.18 (a, b) TEM and HRTEM images, and (c, d) SAED and simulated patterns of image of the product prepared using 5.0 mmol $Sr(NO_3)_2$, $(NH_4)_6Mo_7O_{24}{\cdot}4H_2O$ as starting reagents and a 270 w microwave-hydrothermal for 30 min (Sample code MSA3).

When Sr and Mo solutions were mixed, the intermediate complexes formed. Subsequently, they were processed by the microwave-hydrothermal reaction, and gradually transformed for a few steps into hierarchical nanostructures of $SrMoO_4$ with donut-like or flower-like shape.

$$Sr^{2+} + (Mo_7O_{24})^{6-} \rightarrow \text{ intermediate complexes} \rightarrow SrMoO_4 \text{ (molecules)}$$

$SrMoO_4$ molecules nucleated and grew to form nanoparticles. Furthermore, these nanoparticles selectively grew to form nanosheet petals for the MSA1 to MSA4 and MSC1 to MSC3 products, and nanorod petals for the MSB1 to MSB3 products on top. As the processing time passed, the petals were enlarged and squeezed each other. Some petals were bent and some were broken to release stress energy. The flowers (donuts) became more complete as well. In the end, the particles became completely donut-like shape (Figure 4.4.19).

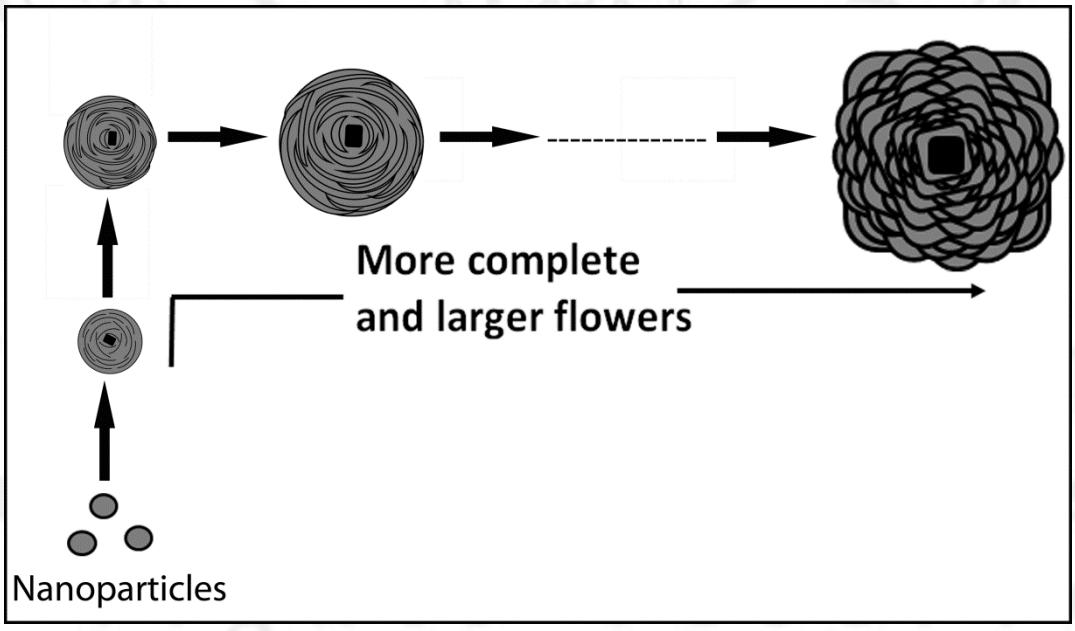

Figure 4.4.19 Schematic illustration for the formation of hierarchical architecture of $SrMoO_4$.

Several different vibrations were detected on Raman spectra of the $SrMoO_4$ crystals (Figure 4.4.20). The Raman peaks at 881 cm^{-1} were specified as the $\nu_1(A_g)$ symmetric stretching vibration mode of $[MoO_4]^{2-}$ units. Those at 838–841 and 788–790 cm^{-1} corresponded to the $\nu_3(B_g)$ and $\nu_3(E_g)$ anti-symmetric stretching vibration modes, respectively. The peaks at 368 and 328–330 cm^{-1}, respectively corresponded to the $\nu_4(B_g)$ anti-symmetric and $\nu_2(A_g)$ symmetric bending modes, including the 181–183 cm^{-1} to the $\nu_{f.r.(}F1)$ free rotation modes. Those at 118, 141 and 163 cm^{-1} were specified as the external vibration modes of Sr^{2+} cations and $[MoO_4]^{2-}$ units. These vibration modes were very close to those reported by other researchers [27, 79, 130], and provided the evidence of scheelite structure.

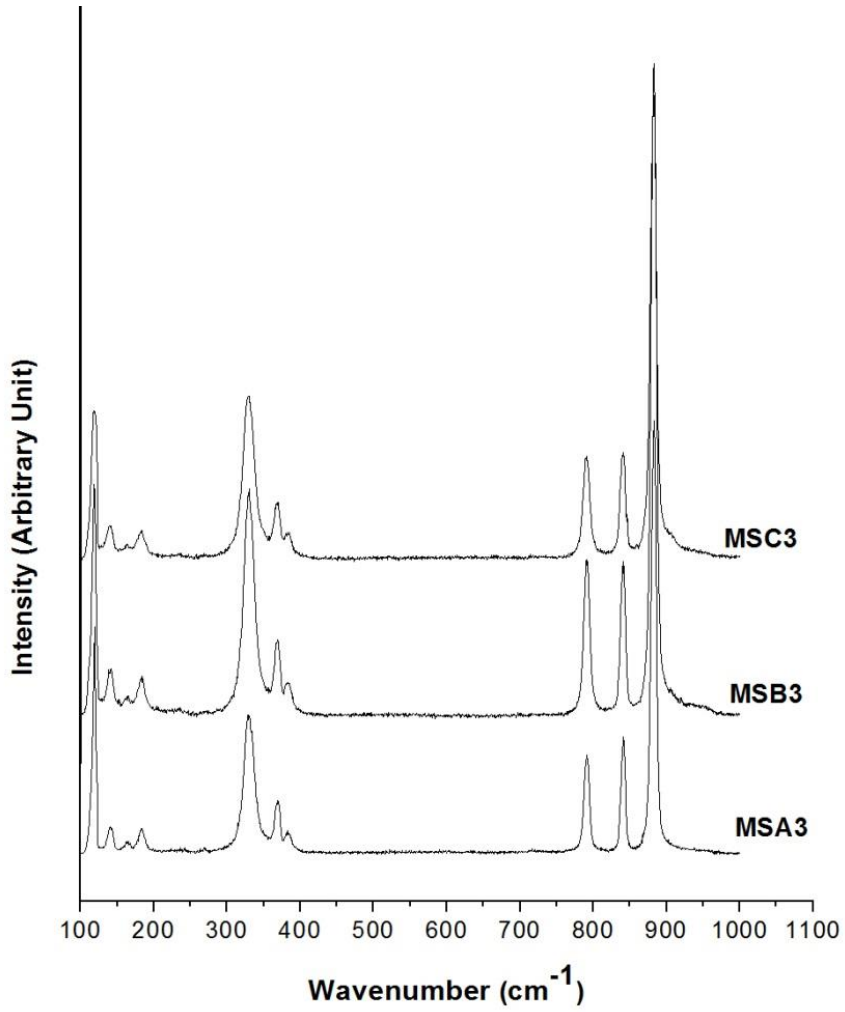

Figure 4.4.20 Raman spectra of the MSA3, MSB3 and MSC3 products, the product prepared using 5.0 mmol $Sr(NO_3)_2$, and $(NH_4)_6Mo_7O_{24}{\cdot}4H_2O$ as starting reagents and a 270 w microwave-hydrothermal for 5, 15, and 30 min respectively.

UV-visible absorption (Figure 4.4.21-4.4.22) of the hierarchical $SrMoO_4$ architecture of the MSC3 product synthesized by the 270 W and 30 min microwave-hydrothermal process indicated an exponential decreasing of the UV-visible energy attenuated through the crystalline MSC3 product. During attenuation, the absorption was controlled by two photon energy (hν) ranges. For $h\nu > E_g$, the absorption was

linearly increased with the increasing of photon energy. The steep inclination of the linear portion of the curve was caused by the UV absorption for charged transition from the topmost occupied state of valence band to the bottommost unoccupied state of the conduction band. For hν < Eg, the absorption curve became different from linearity, caused by the UV absorption for charged transition relating to defects. Band gap of the product is related with its absorbance and photonic energy. Thus the combination of absorbance and photonic energy was used to determine the photonic band gap. By extrapolating the linear portion curve (tail of the curve) of the $(\alpha h\nu)^2$ vs hν plot to zero absorption, its direct energy gap was determined to be 3.92 eV for the hierarchical architecture of the MSC3 product. This energy gap was very close to the 3.98 eV of $SrMoO_4$ powder processed by the microwave-hydrothermal reaction at 413 K for 5 h reported by Sczancoski et al. [27].

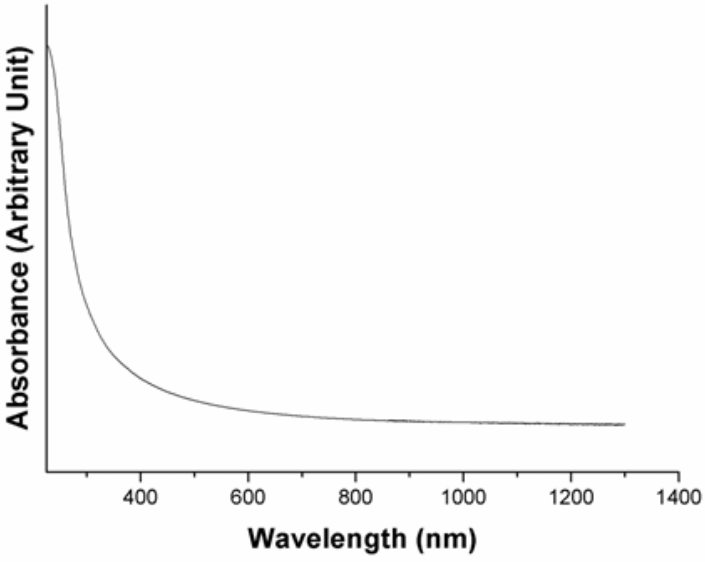

Figure 4.4.21 UV-visible absorption of the MSC3 product, the product prepared using 5.0 mmol $Sr(NO_3)_2$, and $(NH_4)_6Mo_7O_{24}{\cdot}4H_2O$ as starting reagents and a 270 w microwave-hydrothermal for 30 min.

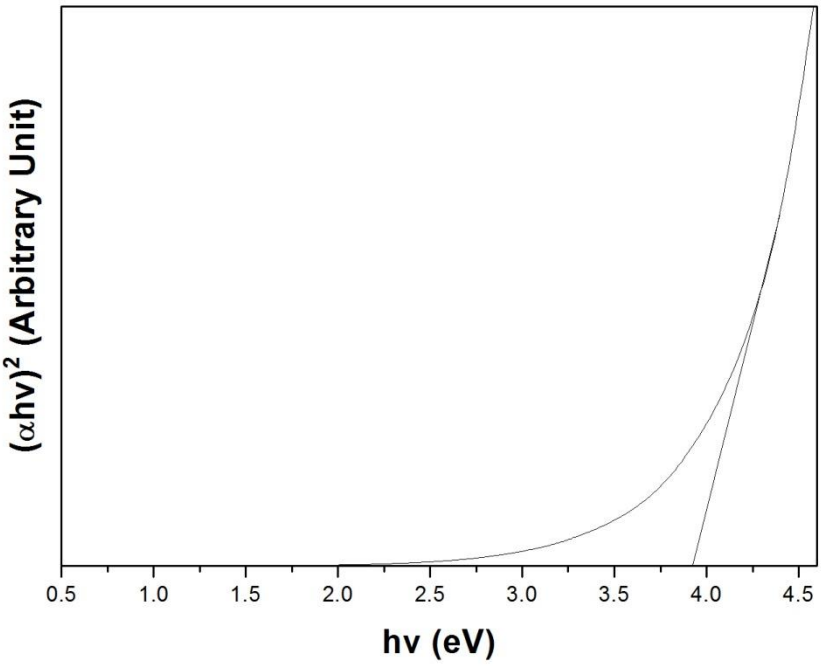

Figure 4.4.22 the $(\alpha h\nu)^2$ vs hν plot of the MSC3 product, the product prepared using 5.0 mmol $Sr(NO_3)_2$, and $(NH_4)_6Mo_7O_{24}{\cdot}4H_2O$ as starting reagents and a 270 w microwave-hydrothermal for 30 min.